QUANTUM CRITICALITY

Tunable quantum criticality and super-ballistic transport in a "charge" Kondo circuit

Z. Iftikhar[1], A. Anthore[1,2], A. K. Mitchell[3], F. D. Parmentier[1]*, U. Gennser[1], A. Ouerghi[1], A. Cavanna[1], C. Mora[4], P. Simon[5], F. Pierre[1]†

Quantum phase transitions (QPTs) are ubiquitous in strongly correlated materials. However, the microscopic complexity of these systems impedes the quantitative understanding of QPTs. We observed and thoroughly analyzed the rich strongly correlated physics in two profoundly dissimilar regimes of quantum criticality. With a circuit implementing a quantum simulator for the three-channel Kondo model, we reveal the universal scalings toward different low-temperature fixed points and along the multiple crossovers from quantum criticality. An unanticipated violation of the maximum conductance for ballistic free electrons is uncovered. The present charge pseudospin implementation of a Kondo impurity opens access to a broad variety of strongly correlated phenomena.

Continuous second-order quantum phase transitions (QPTs)—which take place at absolute zero temperature as a control parameter such as the magnetic field is tuned—are accompanied by the development of a highly correlated quantum critical state. With increasing temperature, this state extends over a broadening range of parameters further away from the critical point. In this regime of quantum criticality, the properties of the system obey scaling laws determined by the QPT universality class and do not depend on microscopic details. Although QPTs are ubiquitous in contemporary theoretical physics and have been observed in a multitude of highly correlated materials (1), it remains challenging to realize them in simple, well-controlled experimental systems.

Tunable nanostructures provide a path to a microscopic understanding of QPTs that circumvents the complexity of real-world highly correlated materials. So far, however, the rare examples that exhibit a second-order QPT (2–6) demonstrate only a single quantum critical point (associated with the two-channel Kondo effect, described below); although it is a non-Fermi liquid, this critical point can be treated with a perturbative approach in the low-temperature limit (7, 8). By contrast, we realized and characterized completely a circuit that embodies the three-channel Kondo model, with three fully tunable channels connected to a magnetic impurity emulated by the charge states of a metallic island. Within the same nanostructure, this gives us access to two universality classes of quantum criticality (associated with the two-channel and three-channel Kondo effects) that manifest profoundly dissimilar physics. For instance, the quantum critical point for two symmetric Kondo channels can be understood in terms of free electrons and Majorana fermions (7, 8), whereas for three symmetric channels, it involves ($\mathbb{Z}_3$) parafermions with irreducibly strong interactions (9). The demonstrated high-precision implementation qualifies our device as an analog quantum simulator, providing quantitative experimental solutions for the three-channel Kondo model.

The multichannel Kondo model

The multichannel Kondo model, which is a generalization of the original (one channel) Kondo model, gives rise to archetypal QPTs and collective, non-Fermi liquid behaviors from a minimal Hamiltonian. Although introduced to account for the different atomic orbitals in metals (10–12), it has developed over the years into a central testing ground for strongly correlated and quantum critical physics and is a benchmark for many-body theoretical methods (7, 11–19). The model describes a local Kondo spin S (of 1/2 here) coupled antiferromagnetically to N independent free-electron continua (Fig. 1A, $N = 3$)

$$H_{\text{NCK}} = \sum_{i=1}^{N} J_i \mathbf{s_i} \cdot \mathbf{S} + H_{\text{continua}} \quad (1)$$

where H_{NCK} is the N-channel Kondo Hamiltonian, $\mathbf{s_i}$ is the local spin density of electron continuum (channel) i at the Kondo spin $\mathbf{S}$ location, $J_i > 0$ is the coupling strengths (here assumed isotropic), and H_{continua} is the free-electron continua Hamiltonian. The conventional single-channel model ($N = 1$) exhibits universal scaling but no second-order QPT or non-Fermi liquid physics. As the temperature T is reduced, the electrons progressively screen the Kondo spin, resulting for $T \to 0$ in an idle spin-singlet (11). By contrast, for $N \geq 2$, there is a competition between channels to screen the $S = 1/2$ Kondo impurity, which develops into second-order QPTs. Each number of identical channels corresponds to a different class of quantum criticality (16), with specific non-Fermi liquid physics (12) and collective excitations revealed by, for example, a divergent specific heat coefficient c/T as $T \to 0$. The marginal two-channel case corresponds to a logarithmic c/T divergence (12), whereas power law c/T divergences are predicted for $N \geq 3$ (12).
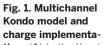
Kondo "charge" pseudospin implementation

Experimentally, Kondo nanostructures are usually small quantum dots (20–23), in which coherent electron cotunneling merges the distinct electrical contacts into one Kondo channel (24, 25) [except in the two-channel devices in (2, 5, 26, 27)]. By contrast, in the recently demonstrated (6) "charge" Kondo approach (14, 28, 29), the charge Kondo impurity S is not a magnetic spin but a pseudospin-1/2 (Fig. 1B, red arrow) built from the macroscopic quantum states describing the overall charge Q of a small metallic island (Fig. 1B, red disk). We extended this concept to three independent Kondo channels. In the most straightforward case of a weakly connected island whose charge is well quantized (30), the Kondo spin $S = \{\downarrow, \uparrow\}$ directly maps on the island's two charge states of lowest energy $\{Q, Q + e\}$. All the other charge configurations are indeed frozen out and can be ignored at low temperatures $T \ll E_C/k_B$ ($E_C = e^2/2C$ is the charging energy, e is the electron charge, C is the island geometric capacitance, and k_B is the Boltzmann constant). The charge pseudospin energy degeneracy is obtained by tuning (with a gate voltage V_g) the device at the degeneracy point between the charge states Q and $Q + e$. Detuning V_g away from charge degeneracy is completely analogous to applying a magnetic field on usual magnetic Kondo impurities (28). The island charge Kondo pseudospin S is, however, not coupled to the real spin of electrons. Instead, it is flipped by transferring electrons in and out of the island, through the connected electrical channels (Fig. 1B, red dashed lines). This mechanism takes the form of a Kondo (pseudo-) spin-exchange coupling: Introducing an electron pseudospin s (Fig. 1B, blue arrow), which corresponds to the electron localization inside ($s = \downarrow$) or outside ($s = \uparrow$) of the island, the tunneling of an electron flips both its localization pseudospin s as well as the island overall charge pseudospin S. A well-developed Kondo effect requires a continuum of electronic states

[1]Centre de Nanosciences et de Nanotechnologies (C2N), CNRS, Univ. Paris-Sud, Université Paris-Saclay, 91120 Palaiseau, France. [2]Univ. Paris Diderot, Sorbonne Paris Cité, 75013 Paris, France. [3]School of Physics, University College Dublin, Dublin 4, Ireland. [4]Laboratoire Pierre Aigrain, Ecole Normale Supérieure–PSL Research University, CNRS, UPMC Univ. Paris 06–Sorbonne Universités, Univ. Paris Diderot-Sorbonne Paris Cité, 75005 Paris, France. [5]Laboratoire de Physique des Solides, CNRS, Univ. Paris-Sud, Université Paris-Saclay, 91405 Orsay, France.
*Present address: Service de Physique de l'État Condensé, CEA, CNRS, Université Paris Saclay, CEA-Saclay 91191 Gif-sur-Yvette, France.
†Corresponding author. Email: frederic.pierre@u-psud.fr

for both localization pseudospins. This implies a continuous density of states in the metallic island (in contrast with small quantum dots). The different conduction channels constitute here separate Kondo channels. Also, the same physics is predicted at $T \ll E_C/k_B$ for arbitrary connection strengths (14, 31, 32), except perfectly ballistic contacts, despite the coexistence of many charge states in a quantum superposition near the ballistic limit (30). In practice, we found from numerical renormalization group (NRG) calculations performed over a broad range of coupling strengths that $T \lesssim E_C/20k_B$ ensures negligible deviations from universal Kondo physics (32).
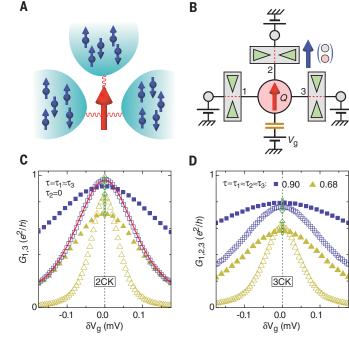
Each of the Kondo/conduction channels passes through a different quantum point contact (QPC) individually formed by means of field effect in a high-mobility Ga(Al)As two-dimensional electron gas (32). Single channels, polarized in real electron spin, are obtained by immersing the device into a large magnetic field ($B \simeq 2.7$ T, corresponding to the regime of the integer quantum Hall effect at filling factor $\nu = 3$). The Kondo channel couplings J_i ($i \in \{1, 2, 3\}$) are individually characterized by the "intrinsic" (unrenormalized by Kondo or Coulomb effects) transmission probability τ_i across the single open transport channel of QPC$_i$. The micrometer-scale separation between QPCs enables independent fine tuning (~0.1%) and high-precision characterization [≤2%, with a large dc bias voltage suppressing Kondo/Coulomb

renormalization (32)] of the Kondo channels, over the full range $\tau_i \in [0, 1]$. Such fine tuning of the connected channels to identical couplings is crucial for approaching the frustrated, symmetric Kondo critical points. The two-channel Kondo (2CK) configurations are implemented by setting $\tau_1 \simeq \tau_3 \equiv \tau$ and $\tau_2 = 0$, whereas for the three-channel Kondo (3CK) configurations $\tau_1 \simeq \tau_2 \simeq \tau_3 \equiv \tau$. With the charging energy $E_C \simeq k_B \times 0.3$ K (separately obtained from Coulomb diamond measurements) and high-precision shot-noise thermometry (33), the device is completely characterized. The knowledge of these parameters allows for a full quantitative microscopic understanding (19, 28, 29). In practice, Kondo physics is observed through the renormalized QPC conductances G_i measured in situ. Because the symmetry between channels is found preserved by renormalization (at an experimental accuracy of ~0.003e^2/h), we generally display the averages $G_{1,3} \equiv (G_1 + G_3)/2$ and $G_{1,2,3} \equiv (G_1 + G_2 + G_3)/3$ when investigating the symmetric 2CK and 3CK configurations, respectively.

The high-precision implementation/quantum simulation of the charge Kondo model is validated in Fig. 1, C and D, and the different two-channel and three-channel Kondo behaviors are qualitatively illustrated. The renormalized conductance across channels tuned to "intrinsic" $\tau \simeq 0.90$ (Fig. 1, C and D, squares) or 0.68 (Fig. 1, C and D, triangles) is displayed for $T \simeq 7.9$ and 29 mK while

sweeping the gate voltage V_g. The charge degeneracy point is identified as the conductance peak ($\delta V_g = 0$). The good match, without any fit parameters, between the conductance data and the quantitative predictions of the charge Kondo model derived analytically for two near ballistic channels at low temperature (Fig. 1C, continuous line) (29, 32) attests to the accurate device characterization and to its precise implementation of the model for arbitrary Kondo pseudospin energy splitting (19, 32). At large δV_g, the conductance is systematically reduced upon lowering T as usually expected from plain charge quantization. At $\delta V_g = 0$ and for two or three symmetric channels set to $\tau \simeq 0.68$, we observed instead a conductance increase with T owing to the Kondo renormalization of weakly connected channels. At the larger $\tau \simeq 0.90$, 2CK and 3CK exhibit qualitatively different conductance renormalizations at $\delta V_g = 0$, with opposite signs.

Observation of an intermediate nontrivial fixed point

The above findings corroborate the theoretical expectations for the different 2CK and 3CK low-temperature conductance fixed points (29, 34). Both 2CK and 3CK quantum critical fixed points are associated with an intermediate value of the renormalized Kondo coupling $0 < |J| < \infty$ (10, 12). In previous experiments on small quantum dots (2, 5), the 2CK intermediate coupling could not be established. Indeed, T was not low enough with respect to the scaling Kondo temperature T_K to show a saturation; furthermore, asymmetries between electrical channels (15) can lead to a trivial intermediate asymptotic value of the measured conductance, which therefore does not necessarily imply an intermediate coupling in these spin Kondo devices. Moreover, the intermediate coupling character of the 2CK fixed point is not entirely invariable but depends on the choice of representation (7, 8, 14, 29). In particular, the 2CK fixed point can be described as a noninteracting system involving two Majorana modes [one free, one in the strong coupling limit (7)]. This dual strong-coupling character of the 2CK fixed point also materializes in the present charge Kondo implementation: Here, $G_{1,3}$ constitutes an alternative probe of the coupling between electrons and charge Kondo impurity, which flows not toward an intermediate value per electrical channel but toward the maximum free-electron quantum limit $G_{2CK} = e^2/h$ (29). By contrast, the genuinely intermediate character of the interacting 3CK fixed point is predicted to show up directly in charge Kondo circuits, as a flow of the conductance per channel $G_{1,2,3}$ toward the nontrivial intermediate universal conductance $G_{3CK} = 2\sin^2(\pi/5)e^2/h \simeq 0.691e^2/h$ (34).

The precise 2CK and 3CK low-temperature universal conductance fixed points are experimentally established by measuring the temperature evolution of $G_{1,3}$ and $G_{1,2,3}$, respectively, for a broad range of symmetric channel settings [$\tau \in (0.56, 0.985)$]. For this purpose, and until explicitly specified otherwise, the device is tuned

Fig. 1. Multichannel Kondo model and charge implementation. (**A**) In the Kondo model, a local spin (red arrow) is antiferromagnetically coupled to the spin of electrons (blue arrows). Each Kondo channel corresponds to one distinct electron continuum (three continua are shown here). (**B**) Sample schematic realizing the charge pseudospin implementation of the three-channel Kondo model. A micrometer-scale metallic island (red disk) is connected to large electrodes (small gray disks) through three QPCs (green split gates),

each set to a single (spin-polarized) conduction channel (red dashed lines) indexed by $i \in \{1, 2, 3\}$. (**C** and **D**) Quantum channels conductance measured versus gate voltage V_g is displayed over half a Coulomb oscillation period $\Delta \simeq 0.7$ mV (several sweeps including different consecutive peaks are averaged). Measurements at $T \simeq 7.9$ and 29 mK are shown, respectively, as open and full symbols for two (C) or three (D) symmetric channels. The squares correspond to an "intrinsic," unrenormalized transmission probability across the connected QPCs of $\tau \simeq 0.90$, and triangles to that of $\tau \simeq 0.68$. The red continuous line (C) displays the $T = 7.9$ mK prediction for two channels both set to $\tau = 0.90$ (32). Green arrows indicate the direction of conductance change at $\delta V_g = 0$ as temperature is reduced.
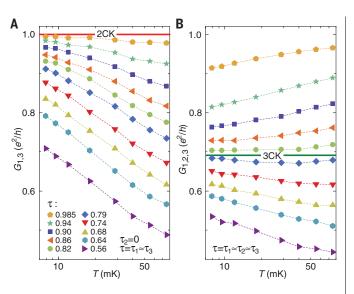
Fig. 2. Quantum critical fixed points. (A and **B)** The conductance of (A) two or (B) three symmetric channels measured at the charge degeneracy point ($\delta V_g = 0$) is plotted as symbols versus temperature on a logarithmic scale. Each set of identical symbols connected by dashed lines corresponds to the same device setting (τ). The predicted (A) 2CK and (B) 3CK l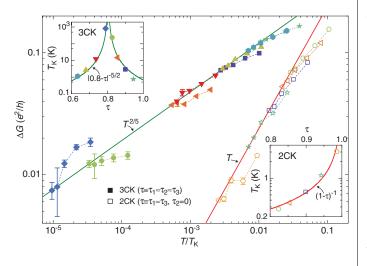ow-temperature fixed points for the conductance per channel in the present charge Kondo implementation are shown as horizontal continuous lines [$G_{2CK} = e^2/h$, $G_{3CK} = 2\sin^2(\pi/5)e^2/h$].

Fig. 3. Non-Fermi liquid scaling exponents. The absolute difference between symmetric channels conductance at charge degeneracy and predicted Kondo fixed point ($\Delta G \equiv |G_{1,3} - G_{2CK}|$ and $\Delta G \equiv |G_{1,2,3} - G_{3CK}|$) is plotted as symbols (open and solid for 2CK and 3CK, respectively) versus T/T_K in a log-log scale for $T \in \{7.9, 9.5, 12, 18, 29\}$ mK. Statistical error bars are shown when larger than symbols. The red and green continuous straight lines display the predicted power-law scaling at $T/T_K \ll 1$ for the conductance per channel in the present charge 2CK and 3CK implementations, respectively. The scaling Kondo temperature T_K is adjusted separately for each tuning τ of the symmetric channels (insets, corresponding symbols). This is done by matching the lowest-temperature data point $\Delta G(T \simeq 7.9$ mk) with the corresponding displayed power law. Continuous lines in insets show the predicted power-law divergences of T_K versus τ for 2CK (bottom right inset) and 3CK (top left inset).

at charge degeneracy ($\delta V_g = 0$), where Kondo effect is expected. Measurements of $G_{1,3}$ and $G_{1,2,3}$ versus T in logarithmic scale are shown as symbols in Fig. 2. In the 2CK configuration (Fig. 2A), whatever the setting τ, we found that $G_{1,3}$ always grows as T is reduced. This observation validates the predicted e^2/h Kondo fixed point (Fig. 2A, horizontal red line), at an experimental accuracy of $0.006e^2/h$ (6). Upon lowering T in the 3CK configuration (Fig. 2B), $G_{1,2,3}$ systematically grows when below $0.68e^2/h$ (and for $T \le 40$ mK) and decreases when above $0.70e^2/h$. This validates the predicted 3CK universal conductance fixed point $G_{3CK} \simeq 0.69e^2/h$ (horizontal green line) at an experimental accuracy of $\pm 0.01e^2/h$. This constitutes direct experimental

evidence of an intermediate non-Fermi liquid fixed point.

Universal scalings toward quantum criticality

First, we characterized the power-law exponents when approaching the 2CK and 3CK low-temperature fixed points and found them to be different from the characteristic T^2 for Fermi liquids. For this purpose, the distances ΔG between measured $G_{1,3}$ and $G_{1,2,3}$ and, respectively, the theoretically predicted fixed points G_{2CK} and G_{3CK} are plotted in Fig. 3 versus T/T_K. The continuous straight lines show the universal power-law scalings asymptotically predicted at low T/T_K for the conductance in the present charge Kondo

implementation: $\Delta G \propto T$ for 2CK (19, 29, 35) and $\Delta G \propto T^{2/5}$ for 3CK (12, 13, 32) [further discussion is provided in (32)]. Comparing with the data requires us to, for each τ, fix the corresponding scaling Kondo temperature $T_K(\tau)$. Symbols in the Fig. 3 insets represent the experimentally extracted values of T_K versus τ, which were obtained for each tuning τ by matching the lowest-temperature data point with the displayed theoretical power law. The data-theory comparison in the main Fig. 3 panel is therefore in the conductance evolution as temperature is increased. We found that sufficiently close to the fixed points ($\Delta G \lesssim 0.1e^2/h$), the experiment is consistent with predictions. The precision is here limited by the increasing relative experimental uncertainty as ΔG is reduced. A direct extraction of the temperature exponents from the $\Delta G < 0.1e^2/h$ data at $T \in \{7.9, 12\}$ mK (satisfying the NRG universality criteria $T \lesssim E_C/20k_B \simeq 15$ mK) gives $\alpha_{2CK} = 0.83 \pm 0.08$ for 2CK and $\alpha_{3CK} = 0.42 \pm 0.17$ for 3CK.

We then investigated the full 2CK and 3CK universal renormalization flows. Measurements (symbols) are now compared in Fig. 4, A to C, with NRG calculations spanning the whole range of T/T_K (Fig. 4, continuous black lines) (32). In Fig. 4, A and B, respectively, $G_{1,3}$ and $G_{1,2,3}$ are plotted versus $\log(T/T_K)$. Following standard procedures, the theoretical scaling Kondo temperature T_K was normalized so that the NRG universal conductance takes a value equal to half that of the Kondo fixed point at $T = T_K$. As in Fig. 3, the experimental $T_K(\tau)$ (symbols in Fig. 4 insets) are adjusted by matching data with theory at $T \simeq 7.9$ mK. These $T_K(\tau)$ remain therefore identical to those in the insets of Fig. 3 as long as NRG calculations and asymptotic power laws are indistinguishable (for $T_K \gg 7.9$ mK). We observed a quantitative agreement between the data and the universal NRG prediction over six (2CK) or eight (3CK) orders of magnitude in T/T_K. A direct comparison of the same measurements and predictions is shown in Fig. 4C in a scale-invariant representation that does not involve rescaling the temperature in units of T_K, by displaying $\partial G_{1,3}/\partial \log(T)$ versus $G_{1,3}$ and $\partial G_{1,2,3}/\partial \log(T)$ versus $G_{1,2,3}$. In this representation, data points correspond to experimental measurements of the so-called β-function that determines the corresponding 2CK or 3CK renormalization group equation for the conductance. In Fig. 4C, the straight dashed lines near 2CK and 3CK fixed points (Fig. 4C, arrows) represent the predicted non-Fermi liquid power-law behaviors discussed in the previous paragraph. Comparing with the experimental slope therefore complements the approach in Fig. 3. Also shown is the experimental "analog quantum simulation" of the universal 3CK β-function at $G_{1,2,3} > G_{3CK}$, out of reach of NRG calculations.

Last, we explored the quantitative relationship between scaling Kondo temperature T_K and microscopic model parameter τ (Figs. 3 and 4, insets). At small $\tau \lesssim 0.5$, the same expected exponential behavior $T_K \simeq (E_C/10k_B)\exp(-\pi^2/\sqrt{4\tau})$ is observed for 2CK and 3CK (29). At larger τ, T_K appears to diverge at a specific setting τ_c, with extracted T_K values orders of magnitude above
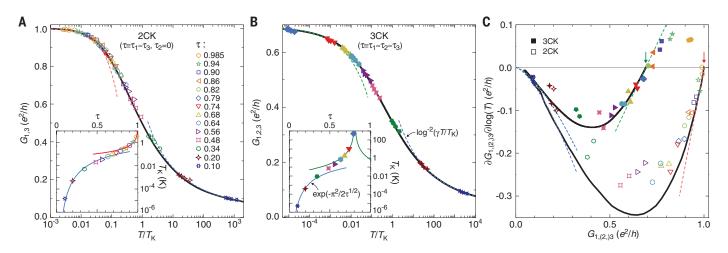
Fig. 4. Universal renormalization flow to quantum criticality. The measured conductance of the two or three connected, symmetric channels is shown as symbols (open and solid for 2CK and 3CK, respectively) for a broad range of settings τ. (**A** and **B**) Data ($T \in \{7.9, 9.5, 12, 18\}$ mK) and predictions are plotted versus T/T_K in log scale. The corresponding experimental T_K are shown in insets as symbols versus τ, together with theoretical predictions for tunnel contacts $\tau \ll 1$ (light-blue continuous lines) and for very large T_K at $|\tau - \tau_c| \ll 1$ [respectively, red and green continuous lines for 2CK and 3CK in insets of (A) and (B)]. (**C**) Direct data-theory comparison (no T/T_{co} rescaling) with $\partial G_{1,3}/\partial \log(T)$ plotted versus $G_{1,3}$ and $\partial G_{1,2,3}/\partial \log(T)$ pl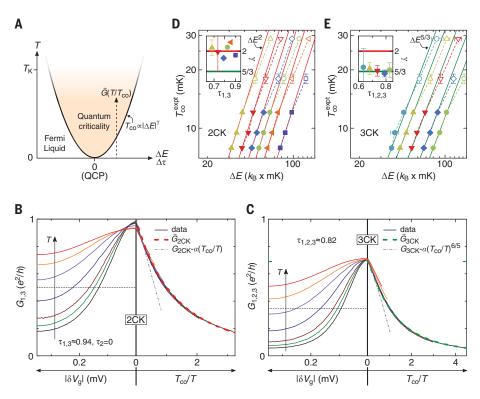otted versus $G_{1,2,3}$. The discrete experimental differentiation is performed with measurements at $T \in \{7.9, 12, 18\}$ mK. Kondo fixed points are indicated by arrows. Black continuous lines are NRG calculations of the universal renormalization flows [2CK in (A) and (C) and 3CK in (B) and (C)]. Colorized dashed lines shown at low T/T_K [(A) and (B)], and close to the Kondo fixed points (C), display the predicted low-temperature power laws for 2CK [red in (A) and (C)] and 3CK [green in (B) and (C)]. Light blue dashed lines shown at large T/T_K [(A) and (B)], and for small channels conductance (C), represent the predicted high-temperature logarithmic scaling proportional to $\log^{-2}(\gamma T/T_K \gg 1)$, with the slightly different 2CK and 3CK prefactors and γ here used as fit parameters.

the high-energy cutoff $E_C/k_B \simeq 300$ mK (in which case, universal Kondo physics can only be probed at $T/T_K \ll 1$). For 2CK, theory predicts a divergence at $\tau_c = 1$ as $T_K(1 - \tau \ll 1) \propto 1/(1 - \tau)$, which is displayed by the identical continuous red lines in the insets of Figs. 3 and 4A (29) [(31, 36), the prediction of a peaked $T_K(J)$]. For 3CK, the observed value $\tau_c \simeq 0.8$ is higher than $G_{3CK}h/e^2 \simeq 0.69$. This is caused by the conductance suppression by Coulomb interaction at temperatures $T \gtrsim E_C/k_B$, before the development of universal Kondo physics at low temperatures. Assuming theoretically that T_K diverges at τ_c, we generally find (32) that a low-temperature conductance power law $\Delta G \propto T^\alpha$ corresponds to a power-law divergence as $T_K \propto |\tau - \tau_c|^{-1/\alpha}$. The observed close agreement between experimental $T_K(|\tau - \tau_c| \ll 1)$ in 2CK and 3CK configurations with, respectively, $T_K \propto |\tau - 1|^{-1}$ (Figs. 3 and 4A, insets, red lines) and $T_K \propto |\tau - 0.8|^{-5/2}$ (Figs. 3 and 4B, insets, green lines) therefore further establishes the predicted non-Fermi liquid Kondo exponents for two ($\alpha_{2CK} = 1$) and three ($\alpha_{3CK} = 2/5$) symmetric channels.

Crossover from quantum criticality

As the temperature is increased [up to some limit; here, $T \lesssim \min(T_K, E_C/k_B)$], the quantum critical regime is generally expected to span over a larger range of system parameters, away from the $T = 0$ quantum critical point (Fig. 5A). The so-called crossover temperature T_{co} delimits quantum criticality from below, with the critical point itself corresponding to $T_{co} = 0$. Generically, the crossover from quantum criticality as temperature is lowered should follow universal curves versus the reduced parameter T/T_{co}. Indeed, T_{co}

is the only relevant temperature scale, encapsulating all microscopic details, provided that the high-energy cutoff for quantum criticality is much higher. In tunable circuits, the crossover from 2CK quantum criticality was explored versus Kondo channels asymmetry (5, 6) and, in the different implementation of a spin-polarized quantum dot embedded into a dissipative circuit, versus the difference between resonant dot level and Fermi energy (4). These experiments corroborate the existence of a universal T/T_{co} scaling, as well as the predicted quadratic increase of T_{co} for small deviations from the 2CK critical point (12, 15, 18). We explored the disparate universal and exotic behaviors along the different crossovers induced by breaking the Kondo (pseudo)spin degeneracy or the channel symmetry, observed the development of the quantum phase transition across the symmetric 3CK quantum critical point, and demonstrated "super-ballistic" conductances.

In a first step, we investigated the so-far-unexplored crossover from 2CK and 3CK quantum criticality induced by breaking the energy degeneracy of the Kondo impurity, with the connected channels remaining symmetric. We established (i) the different 2CK and 3CK power-law dependence $T_{co} \propto |\Delta E|^\gamma$ for small energy splitting of the charge pseudospin $\Delta E = 2E_C\delta V_g/\Delta \ll E_C$, with $\Delta \simeq 0.7$ mV being the gate voltage period; (ii) a generalized expression of T_{co} for arbitrary ΔE; and (iii) the theoretical universal crossover curves $\tilde{G}_{2CK}(T/T_{co})$ and $\tilde{G}_{3CK}(T/T_{co})$, obtained analytically in (19, 29) for 2CK and by NRG here for 3CK.

The crossover temperature T_{co} is defined so that the conductance is halfway between the

quantum critical regime ($\approx G_{2CK}$ or $\approx G_{3CK}$, at $T_{co} \ll T \ll T_K$) and the Fermi liquid regime (≈ 0, at $T_{co} \gg T$)—that is, $G_{1,3}(\Delta E, T = T_{co}) \equiv G_{2CK}/2$ or $G_{1,2,3}(\Delta E, T = T_{co}) \equiv G_{3CK}/2$. In practice, we fixed the electronic temperature T and adjusted the energy splitting $\Delta E \propto \delta V_g$ in order to obtain this midway conductance value, if possible. In Fig. 5, B and C, this corresponds to the crossings between continuous and horizontal dashed lines, where the experimentally extracted crossover temperature directly reads $T_{co}^{expt}(\Delta E) = T$. Symbols in Fig. 5, D and E, display T_{co}^{expt} versus ΔE for the settings τ where $T_{co} \propto \Delta E^\gamma$ is expected (32). The predicted corresponding power laws are shown as continuous lines ($T_{co} \propto \Delta E^2$ for 2CK, $T_{co} \propto \Delta E^{5/3}$ for 3CK) (12). Fitting separately, for each τ, the $T_{co}^{expt}(\Delta E) \leq 12$ mK data (fulfilling the universality NRG criteria) yield the values of γ displayed as symbols in the insets of Fig. 5, D and E. A statistical analysis of these values gives $\gamma_{2CK} = 2.01 \pm 0.04$ and $\gamma_{3CK} = 1.69 \pm 0.02$ for the crossovers from 2CK and 3CK, respectively, which is in close agreement with theory.

The theoretically predicted universal crossover curves $\tilde{G}_{2CK}(T_{co}/T)$ and $\tilde{G}_{3CK}(T_{co}/T)$, shown as thick dashed lines in Fig. 5, B and C, right hand sides, are compared with conductance data. Continuous lines in Fig. 5, B and C, left hand sides represent the conductance measured at different temperatures versus gate voltage for $\tau_{1,3} \simeq 0.94$ (Fig. 5B) and $\tau_{1,2,3} \simeq 0.82$ (Fig. 5C). These settings correspond to well-developed quantum critical regimes $T \ll T_K$ (small ΔG), a necessary condition to investigate $\tilde{G}_{2CK}$ and $\tilde{G}_{3CK}$ down to small T_{co}/T. In Fig. 5, B and C, right hand sides, the gate voltage sweeps at different temperatures

Fig. 5. Crossover from quantum criticality by pseudospin degeneracy breaking.
(**A**) Quantum criticality extends as T rises. It is delimited from below by the crossover temperature T_{co}, which increases as a power law for small parameter-space distances from the critical point (for example, charge pseudospin energy splitting $\Delta E \propto \delta V_g$, channels asymmetry $\Delta \tau$). Along the crossover, theory predicts universal T/T_{co} scalings [for example, $G_i(T, \Delta E) = \tilde{G}(T/T_{co})$]. (**B** and **C**) The conductance of (B) two and (C) three symmetric channels set, respectively, to $\tau_{1,3} \simeq 0.94$ and $\tau_{1,2,3} \simeq 0.82$, are plotted as continuous lines versus $|\delta V_g|$ (left side) and T_{co}/T (right side) for $T \in \{7.9, 9.5, 12, 18, 29, 40, 55\}$ mK. Colored thick dashed lines (gray dash-dotted lines) shown in right sides display the theoretical universal crossover curves $\tilde{G}_{2CK}$ and $\tilde{G}_{3CK}$ (the predicted $T_{co}/T \ll 1$ power laws). The only fit parameter is an unknown fixed prefactor for the 3CK crossover scale T_{co} [no fit parameters in (B)]. (**D** and **E**) Experimental crossover temperatures T_{co}^{expt} are plotted as symbols in a log-log scale versus ΔE, for (D) two and (E) three symmetric channels. Each set of symbols connected by dashed lines represents one device setting $\tau_{1,3}$ or $\tau_{1,2,3}$ (insets). Full symbols correspond to $T_{co}^{expt} \le 12$ mK. Straight continuous lines display the predicted power laws $T_{co} \propto \Delta E^\gamma$, with $\gamma = 2$ for 2CK and $\gamma = 5/3$ for 3CK. Fitting $T_{co}^{expt}(\Delta E) \le 12$ mK separately for each τ yields the values of γ shown as symbols in the insets with the fit standard error.

(continuous lines) fall on top of one another when plotted versus calculated T_{co}/T, demonstrating the predicted universal character of the crossover from quantum criticality. Moreover, we found a precise match between experimental universal curves and theoretical predictions $\tilde{G}_{2CK}$ and $\tilde{G}_{3CK}$. T_{co} is obtained from experimental parameters by using generalized expressions that remain valid for arbitrary gate voltage beyond the power law at small detuning. For the charge 2CK device with near ballistic channels, the full quantitative expression derived in (29) was used in Fig. 5B: $T_{co} \simeq 1.444 E_C (1 - \tau_{1,3}) \sin^2(\pi \delta V_g/\Delta)$. The data-$\tilde{G}_{2CK}$ comparison in Fig. 5B is therefore without any fit parameter. For 3CK, we expect from NRG calculations the similar generalization $T_{co} = \lambda_{3CK} \sin^{5/3}(\pi \delta V_g/\Delta)$ (32), which was used in Fig. 5C. Because the prefactor $\lambda_{3CK}(\tau, E_C)$ is not known, the value $\lambda_{3CK} = 36$ mK was freely adjusted in the data-$\tilde{G}_{3CK}$ comparison shown in Fig. 5C.

In a second step, the development of the 3CK QPT driven by the channels' competition to screen the Kondo spin is plainly observed through the conductance renormalization flow of asymmetric channels upon lowering temperature (Fig. 6). The Kondo charge pseudospin is energy degenerate ($\delta V_g = 0$), QPC$_{1,3}$ are tuned symmetric ($\tau_1 \simeq \tau_3$), and τ_2 is adjusted separately. Displayed in Fig. 6 as colored lines with arrowheads is the temperature evolution of the measured conductances G_2 (vertical axis) and $G_{1,3}$ (horizontal axis) from 55 to 7.9 mK (arrowhead at lowest T); each line corresponds to a different device setting. In total, 15 × 14 settings of

$\{\tau_2, \tau_1 \simeq \tau_3\}$ were measured, with $\tau_{1,2,3}$ picked among 14 fixed values ranging from 0.1 to 0.985 (32) and including also $\tau_2 = 0$. The data closest to the Fig. 6 diagonal gray line correspond to three channels tuned symmetric ($\tau_1 \simeq \tau_2 \simeq \tau_3$). Below the diagonal, where $\tau_2 < \tau_1 \simeq \tau_3$, the data flow toward the predicted 2CK fixed point (Fig. 6, red disk, at $G_{1,3} = e^2/h$ and $G_2 = 0$). Above the diagonal, where $\tau_2 < \tau_1 \simeq \tau_3$ so that a flow toward the 1CK fixed point involving QPC$_2$ is expected (blue disk, at $G_{1,2,3} = 0$), we observed a monotonous decrease of the conductance $G_{1,3}$ across the less strongly coupled QPCs. By contrast, G_2 first rises, markedly oversteps the free-electron quantum limit e^2/h (up to +25%), and then decreases toward the zero conductance 1CK fixed point as T is further reduced.

The nonmonotonous behavior of G_2 when higher than $G_{1,3}$ might appear counterintuitive. A flow toward the low-temperature 1CK "strong coupling" fixed point is expected, which corresponds to a renormalized Kondo coupling growing monotonously ($J_2 \to \infty$). However, J_2 connects with the tunnel coupling/hopping integral of electrons across QPC$_2$ in the charge Kondo mapping, and free-electron theory predicts a nonmonotonous dependence of the conductance with the hopping integral [with a maximum for the value that best preserves translational invariance, and $G_2(J_2 \to \infty) = 0$]. By contrast, the present measurement of a conductance that exceeds the maximum possible value for noninteracting electrons in the ballistic limit is highly nontrivial and was not anticipated (although reproduced by our

NRG calculations). Such a super-ballistic conductance, also in an intermediate temperature range and of similar amplitude, was coincidently observed in clean graphene constrictions (37) and explained as a collective viscous flow of the electronic fluid induced by electron-electron collisions (38). We speculate that the electron-electron interactions mediated by the Kondo impurity within the electronic channel across QPC$_2$, expected to be particularly strong near the turning point where G_2 is maximum, might also result in such a viscous electronic fluid behavior. One specificity of our system is that the super-ballistic magnitude and the temperature range in which it takes place can be controlled in situ, by separately adjusting the channels.

The experimental findings are compared with NRG calculations of the universal crossover flow from 3CK quantum criticality, induced by an initially minute asymmetry between G_2 and $G_{1,3}$ (32). These are displayed in Fig. 6 as two thick gray lines originating from the 3CK fixed point, with arrows pointing toward lower temperatures. For $G_{1,3} > G_2$, NRG predicts a monotonous crossover flow from 3CK to 2CK conductance fixed points that closely matches the nearby data. For $G_2 > G_{1,3}$, the universal NRG crossover flow from 3CK to 1CK reproduces the observed nonmonotonous behavior, confirms the naively expected vanishing of G_2 at the 1CK fixed point, and establishes that a super-ballistic conductance exceeding by ~20% the free-electron maximum limit follows from the 3CK model, which is in quantitative agreement with the experiment.
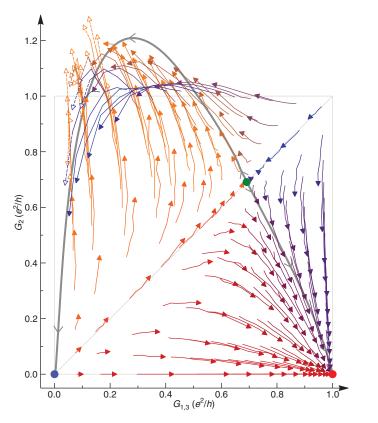
Fig. 6. Three-channel Kondo renormalization flow with super-ballistic conductances. Each colored line with an arrowhead displays the measured channels' conductance at $T = 55, 40, 29, 18, 12$, and 7.9 mK (arrowhead is shown at lowest T) for a fixed device tuning ($\tau_1 \approx \tau_3, \tau_2$) at charge degeneracy ($\delta V_g = 0$). The lines' colors reflect the direction (the angle) of the vector connecting lowest- and highest-temperature data points, to improve readability. Because QPC$_1$ and QPC$_3$ are set symmetric [$\tau_1 \approx \tau_3$ tuned among 14 values from 0.1 to 0.985 (32)], only the renormalized average $G_{1,3}$ is shown on the horizontal axis. QPC$_2$ is separately adjusted to a coupling τ_2 selected among the same 14 values and also $\tau_2 = 0$. For the solid lines and solid arrows, the experimental standard error of $G_2 h/e^2$ and $G_{1,3} h/e^2$ is below 0.05 (usually well below). For the dashed lines and open arrows, the standard error of $G_2 h/e^2$ is between 0.05 and 0.1. The green, red, and blue disks correspond, respectively, to the predicted 3CK, 2CK, and 1CK low-temperature fixed points. The thick gray lines represent NRG calculations of the universal crossover flows from 3CK (32), with arrows pointing to lower temperatures. The conductance G_2 can markedly exceed the maximum free electron limit e^2/h.

Although experimental and NRG flows point to the same direction near 3CK and 1CK fixed points, clear crossings are also visible in intermediate regimes above the diagonal, including between different experimental device settings. These mostly take place between flows involving opposite renormalization directions of G_2, as expected from the nonmonotonous relationship between G_2 and Kondo coupling J_2 that specifically shows up above the diagonal.

Outlook

The observation of super-ballistic conductance opens a research path for low-power electronics. Although the present implementation has no clear application potential, it forms a powerful platform from which to understand the underlying mechanisms of behaviors that arise in diverse clean systems with strong electron-electron interactions. We anticipate that similar metal-semiconductor hybrids will form building blocks

for a wide range of investigations of the strongly correlated electron physics, and in particular the emergence of exotic parafermion quasi-particles (7, 9, 35). Measurements of complementary observables—such as charge susceptibility, fluctuations, and heat current—as well as investigations of the dynamical and out-of-equilibrium responses could unveil yet hidden facets of the exotic underlying physics. Furthermore, direct generalizations of the present charge Kondo implementation should grant access to quantitative investigations of many thus-far-inaccessible strongly correlated phenomena (16, 39), including the nanoengineered competition between Kondo channels, dissipation [specific proposal in (40)], fractional quantum Hall effect, and multiple impurities.

REFERENCES AND NOTES

1. S. Sachdev, *Quantum Phase Transitions* (Cambridge Univ. Press, 2011).
2. R. M. Potok, I. G. Rau, H. Shtrikman, Y. Oreg, D. Goldhaber-Gordon, *Nature* **446**, 167–171 (2007).
3. H. T. Mebrahtu *et al.*, *Nature* **488**, 61–64 (2012).
4. H. Mebrahtu *et al.*, *Nat. Phys.* **9**, 732–737 (2013).
5. A. J. Keller *et al.*, *Nature* **526**, 237–240 (2015).
6. Z. Iftikhar *et al.*, *Nature* **526**, 233–236 (2015).
7. V. J. Emery, S. Kivelson, *Phys. Rev. B Condens. Matter* **46**, 10812–10817 (1992).
8. P. Coleman, L. B. Ioffe, A. M. Tsvelik, *Phys. Rev. B Condens. Matter* **52**, 6611–6627 (1995).
9. I. Affleck, M. Oshikawa, H. Saleur, *Nucl. Phys. B* **594**, 535–606 (2001).
10. P. Nozières, A. Blandin, *J. Phys.* **41**, 193–211 (1980).
11. A. C. Hewson, *The Kondo Problem to Heavy Fermions* (Cambridge Univ. Press, 1997).
12. D. L. Cox, A. Zawadowski, *Adv. Phys.* **47**, 599–942 (1998).
13. I. Affleck, A. W. W. Ludwig, *Phys. Rev. B Condens. Matter* **48**, 7297–7321 (1993).
14. K. A. Matveev, *Phys. Rev. B Condens. Matter* **51**, 1743–1751 (1995).
15. M. Pustilnik, L. Borda, L. I. Glazman, J. von Delft, *Phys. Rev. B* **69**, 115316 (2004).
16. M. Vojta, *Philos. Mag.* **86**, 1807–1846 (2006).
17. R. Bulla, T. A. Costi, T. Pruschke, *Rev. Mod. Phys.* **80**, 395–450 (2008).
18. E. Sela, A. K. Mitchell, L. Fritz, *Phys. Rev. Lett.* **106**, 147202 (2011).
19. A. K. Mitchell, L. A. Landau, L. Fritz, E. Sela, *Phys. Rev. Lett.* **116**, 157202 (2016).
20. D. Goldhaber-Gordon *et al.*, *Nature* **391**, 156–159 (1998).
21. S. M. Cronenwett, T. H. Oosterkamp, L. P. Kouwenhoven, *Science* **281**, 540–544 (1998).
22. J. Nygård, D. H. Cobden, P. E. Lindelof, *Nature* **408**, 342–346 (2000).
23. M. R. Buitelaar, A. Bachtold, T. Nussbaumer, M. Iqbal, C. Schönenberger, *Phys. Rev. Lett.* **88**, 156801 (2002).
24. L. I. Glazman, M. E. Raikh, *JETP Lett.* **47**, 452 (1988).
25. T. K. Ng, P. A. Lee, *Phys. Rev. Lett.* **61**, 1768–1771 (1988).
26. Y. Oreg, D. Goldhaber-Gordon, *Phys. Rev. Lett.* **90**, 136602 (2003).
27. S. Florens, P. Simon, S. Andergassen, D. Feinberg, *Phys. Rev. B* **75**, 155321 (2007).
28. K. A. Matveev, *Sov. Phys. JETP* **72**, 892 (1991).
29. A. Furusaki, K. A. Matveev, *Phys. Rev. B Condens. Matter* **52**, 16676–16695 (1995).
30. S. Jezouin *et al.*, *Nature* **536**, 58–62 (2016).
31. E. Lebanon, A. Schiller, F. B. Anders, *Phys. Rev. B* **68**, 041311 (2003).
32. Materials and methods are available as supplementary materials.
33. Z. Iftikhar *et al.*, *Nat. Commun.* **7**, 12908 (2016).
34. H. Yi, C. L. Kane, *Phys. Rev. B* **57**, R5579–R5582 (1998).
35. L. Landau, E. Cornfeld, E. Sela, Charge fractionalization in a Kondo device. *Phys. Rev. Lett.* **120**, 186801 (2018).
36. C. Kolf, J. Kroha, *Phys. Rev. B* **75**, 045129 (2007).
37. R. Krishna Kumar *et al.*, *Nat. Phys.* **13**, 1182–1185 (2017).
38. H. Guo, H. Ilseven, G. Falkovich, L. S. Levitov, *Proc. Natl. Acad. Sci. U.S.A.* **114**, 3068–3073 (2017).
39. G. Kotliar, D. Vollhardt, *Phys. Today* **57**, 53–59 (2004).
40. K. Le Hur, *Phys. Rev. Lett.* **92**, 196804 (2004).

Science

Tunable quantum criticality and super-ballistic transport in a "charge" Kondo circuit

Z. Iftikhar, A. Anthore, A. K. Mitchell, F. D. Parmentier, U. Gennser, A. Ouerghi, A. Cavanna, C. Mora, P. Simon and F. Pierre

A nanostructure quantum simulator

Phase transitions occurring at absolute zero temperature, or quantum phase transitions (QPTs), can be grouped into broad categories called universality classes. The classification is based on the properties of the transition rather than the microscopic details of the underlying system. Iftikhar *et al.* exploited this fact to study QPTs in clean, tunable nanostructures, rather than in complex materials, where they most often occur. Within a single nanostructure, two different classes of QPTs with profoundly different characters were studied and comprehensively characterized.

Science, this issue p. 1315

ARTICLE TOOLS	http://science.sciencemag.org/content/360/6395/1315
SUPPLEMENTARY MATERIALS	http://science.sciencemag.org/content/suppl/2018/05/02/science.aan5592.DC1
REFERENCES	This article cites 46 articles, 3 of which you can access for free http://science.sciencemag.org/content/360/6395/1315#BIBL
PERMISSIONS	http://www.sciencemag.org/help/reprints-and-permissions

Supplementary Material for

Tunable quantum criticality and super-ballistic transport in a "charge" Kondo circuit

Z. Iftikhar, A. Anthore, A. K. Mitchell, F. D. Parmentier, U. Gennser, A. Ouerghi,
A. Cavanna, C. Mora, P. Simon, F. Pierre*

*Corresponding author. Email: frederic.pierre@u-psud.fr

This PDF file includes:

> Materials and Methods
> Supplementary Text
> Figs. S1 to S5
> References

Other Supplementary Material for this manuscript includes the following:
(available at www.sciencemag.org/content/science.aan5592/DC1)

> Data File S1 as a separate .zip file

Materials and Methods

1   Sample and setup

Sample. The sample was nanostructured by standard e-beam lithography in a Ga(Al)As two-dimensional electron gas located 105 nm below the surface, of density $2.5\,10^{11}\,\mathrm{cm}^{-2}$ and mobility $10^6\,\mathrm{cm^2V^{-1}s^{-1}}$. The ohmic contact between the micrometer-scale metallic node/'island' and the buried two-dimensional electron gas was realized by thermal diffusion into the semiconductor of a metallic multilayer of nickel (30 nm), gold (120 nm) and germanium (60 nm). The typical energy spacing between electronic levels in the central metallic island is $\delta \approx k_\mathrm{B} \times 0.2\,\mu\mathrm{K}$. The measurements were performed under a strong magnetic field $B \approx 2.7\,\mathrm{T}$, in the regime of the integer quantum Hall effect at filling factor $\nu = 3$. This specific choice was driven by the need to have simultaneously three well-behaved QPCs, without sharp resonances over the full range $\tau \in [0, 1]$, as well as very low temperatures (vibrations in our setup increase the temperature at high field, see (*33*)) and good ohmic contacts between the outer edge channel and the metallic island. The interface quality between metallic island and two-dimensional electron gas is characterized by a residual reflection probability lower than $4\,10^{-4}$ for each of the outermost quantum Hall edge channels originating from the three QPCs. The charging energy $E_\mathrm{C} = e^2/2C \approx k_\mathrm{B} \times 299 \pm 5\,\mathrm{mK} \approx 25.8 \pm 0.5\,\mu\mathrm{eV}$ is obtained from the half-height in drain-source dc bias voltage of measured Coulomb diamonds (not shown, the uncertainties are rough estimates based on four different measurements).

Experimental setup. The device was installed in a dilution refrigerator including multiple filters along the electrical lines and two shields at the mixing chamber. Details on the fridge wiring and on the sample holder are provided in (*33*). Conductance measurements were carried out by standard lock-in techniques at low frequencies, below 200 Hz (see sample micrograph with a schematic measurement setup in Fig. S1). The amplification gains and injected signals are precisely calibrated on-chip, from the signal measured with the QPCs closed ($\tau = 0$). Noise measurements for the electronic thermometry were performed in the MHz range using a homemade cryogenic amplifier. Details on a very similar noise measurement setup can be found in the supplementary materials of (*41*).

2   Experimental methods

Electronic temperature. Below 50 mK, the electronic temperature was extracted on-chip using quantum shot-noise primary thermometry (*33*). Above 50 mK, T is given by a standard ($\mathrm{RuO_2}$) thermometer thermally anchored to the mixing chamber of the dilution refrigerator. From shot-noise thermometry, we obtain for the data points used in the paper $T = \{7.9 \pm 0.1, 9.5 \pm 0.2, 12.1 \pm 0.2, 18 \pm 1, 28.9 \pm 0.8, 40.1 \pm 0.4\}\,\mathrm{mK}$ with the uncertainty corresponding to the standard error on the mean value of T determined from the statistical analysis of several temperature measurements (typically 10). From $\mathrm{RuO_2}$ thermometry, we obtain $T = \{40.3 \pm 0.2, 55.1 \pm 0.3, 75.4 \pm 0.6\}\,\mathrm{mK}$ with the displayed uncertainty corresponding to the temperature drift during the measurements. Note the good agreement

between the two thermometry methods at $40\,\mathrm{mK}$.

Quantum point contact characterization. As generally observed in the integer quantum Hall regime, the conductance across each QPC shows a broad and very well defined e^2/h plateau when varying the corresponding split gate voltage (see inset in Fig. S2E for a gate voltage sweep of QPC_2 including several plateaus). Tuning the QPC to a conductance below e^2/h corresponds to partially opening a single (spin polarized) electronic channel. We extract its 'intrinsic' transmission probability τ essentially by applying a large dc bias voltage ($\sim 50\,\mu\mathrm{V}$) that suppresses the Kondo and Coulomb conductance renormalizations, such that $\tau \simeq Gh/e^2$.

The precise procedure is now described in more details. For characterizing QPC_i ($i \in \{1,2,3\}$), we close $\mathrm{QPC}_{j\neq i}$ ($G_{j\neq i} = 0$) and tune a continuous lateral gate on the other side of the metallic island in the middle of a very broad conductance plateau for which two edge channels are perfectly transmitted (the orange gate in Fig. S1 for $i \in \{1,3\}$, the uncolorized gate for $i = 2$). Note that the small capacitive crosstalk effect on the characterized QPC is compensated (see next section). A very well defined and voltage independent (in the probed range) $h/2e^2$ resistor is therefore in series with QPC_i, as schematically represented in Fig. S2A. Applying a dc voltage V_{dc} across the whole device suppresses the low bias dynamical Coulomb blockade reduction of G_i (see e.g. (*42*) for a theoretical description of dynamical Coulomb blockade), as can directly be seen Fig. S2B. The 'intrinsic' transmission probability τ_i is here identified with the differential conductance G_i measured at large bias voltage (compared to E_{C}/e). The corresponding $G_i(V_{\mathrm{dc}})$ data at $T = 18\,\mathrm{mK}$ are shown as continuous lines in Fig. S2B for the different device settings (black, red, blue for $i = 1,2,3$, respectively). In practice, we extract τ_i from the average of $G_i(V_{\mathrm{dc}})$ in the range $|V_{\mathrm{dc}}| \in [45,51]\,\mu\mathrm{V}$ (grey bands in Fig. S2B). This choice reflects a good compromise between completely suppressing the dynamical Coulomb blockade renormalization (large enough $|V_{\mathrm{dc}}|$) and making sure that the energy dependence of the intrinsic τ_i remains negligible (small enough $|V_{\mathrm{dc}}|$). Note that the symmetry between QPCs was finely adjusted directly from the conductances measured in the 3CK configuration at the specific temperature $T = 18\,\mathrm{mK}$. At large $|V_{\mathrm{dc}}| \gtrsim 20\,\mu\mathrm{V}$, visible differences develop both between QPCs as well as between opposite voltages for the same QPC. We attribute these differences to the small but non-negligible energy dependence of τ_i, which effectively results in an experimental uncertainty on the determination of its absolute value. The corresponding uncertainty is estimated from the standard error $\Delta\tau$ on the mean value τ determined from the six measurements $G_{1,2,3}(V_{\mathrm{dc}} \in \pm[45,51]\,\mu\mathrm{V})$ (three QPCs tuned symmetric at low bias, each measured separately for large positive and negative bias voltages). The mean τ are shown as horizontal dashed lines in Fig. S2B. The extracted values of $\tau_{1,2,3}$, τ and $\Delta\tau$ are recapitulated in the table shown Fig. S2C. Figure S2D,E,F display $\tau_{1,2,3}$ as symbols versus the voltage $V^{\mathrm{qpc}}_{1,2,3}$ applied on one side of the split gate controlling $\mathrm{QPC}_{1,2,3}$, respectively. In order to illustrate the regular gate voltage dependence, continuous traces in the same panels display gate voltage sweeps of the corresponding QPC conductance, with an essentially suppressed dynamical Coulomb blockade renormalization (short-circuiting the island in panels D,E; with a dc voltage of $-50\,\mu\mathrm{V}$ in panel F).

3

Capacitive crosstalk corrections. Each QPC is slightly impacted by the gate voltages applied to control the other QPCs. Thanks to a distance of several microns this capacitive crosstalk is relatively small. Typically, changing the voltage on the other QPCs' split gates has an effect 100 times smaller than directly changing the voltage of the split gate used to form the considered QPC. Although small (the effect on τ is at the most, and generally well below, 0.05), these capacitive crosstalk corrections were straightforwardly calibrated and systematically corrected for, in order to best preserve the QPCs symmetry. Typically, spanning τ on one QPC amounts to gate voltage variations below $0.1\,\mathrm{V}$, resulting in crosstalk corrections smaller than $1\,\mathrm{mV}$ on the other QPCs split gate.

Renormalized channel conductance. Here we detail the relation between individual QPC conductances and the currents and voltages across the whole 'charge' Kondo device. Applying a small voltage V_1 ($eV_1 < k_{\mathrm{B}}T/2$) on the large voltage biased electrode feeding QPC_1 (see Fig. S1), we measure the current I_1 flowing through QPC_1 toward the large grounded electrodes on the other sides of QPC_2 and QPC_3. From Kirchoff's laws, $I_1/V_1 = 1/(1/G_1 + 1/(G_2 + G_3))$. Repeating the same procedure for the three QPCs (in practice this is done simultaneously using lock-in techniques), allows us to extract the individual values of G_1, G_2 and G_3 as long as the three conductances are non-zero, in the 3CK configurations. Note that in the 2CK configurations ($G_2 = 0$), the redundant measurements $I_1/V_1 = I_3/V_3 \equiv G_{1,3}/2$ do not allow us to extract separately G_1 and G_3.

Data reproducibility. The experimental data shown in Fig. 2, 3, 4 and 6 are extracted from the average of the conductance at degeneracy ($\delta V_g = 0$) obtained from many Coulomb peaks. Considering only the symmetric 2CK and 3CK device configurations, a total of 6074 conductance peaks were measured, corresponding in average to 27 peaks per displayed data point. This allowed for the automatic detection and exclusion of statistically anomalous measurements (of statistical probability $\lesssim 1\%$ assuming a gaussian distribution). The excluded measurement artifacts and the automatic procedure are illustrated in Fig. S3. Symbols represent measurements of the maximum peak conductance (at $\delta V_g = 0$) across the whole device when the current is injected from the electrode connected to QPC_2 ($g_{2-13} \equiv 1/(1/G_2 + 1/(G_1 + G_3))$). The data points obtained by sweeping the gate voltage (V_g) at $T \simeq 12\,\mathrm{mK}$ and $\tau \simeq 0.1$ are plotted versus V_g at the position of the consecutive peak maximums. The same sweep was performed twice with a 15h time interval. While in the first sweep (full symbols) all the maximum peak conductances are at similar values, the second sweep (open symbols) shows a pronounced dip of the measured conductance maximums for $V_g \in [-0.402, -0.393]\,\mathrm{V}$. Such non-reproducible experimental artifacts are attributed to the activation of charge fluctuators in the device vicinity. In order to discard such dip artifacts, we automatically remove all peak measurements whose conductance is more than six times the expected standard deviation (from instrumental noise, separately calibrated) below the highest measured value. The highest value and the corresponding lower threshold are shown in Fig. S3 as a black dashed line and a red continuous line, respectively.

Power-law exponent of crossover temperature. This section concerns the experimental determination of the power-law exponent γ describing the increase of the crossover temperature T_{co} versus the charge pseudospin energy splitting ΔE (Fig. 5D,E). We provide here the explicit device settings criteria used to restrict the analysis where such power-law behavior is expected. Two additional criteria complement the already mentioned low temperatures corresponding to the universality regime ($T \leq 12\,\mathrm{mK} < E_{\mathrm{C}}/20 \simeq 15\,\mathrm{mK}$): (*i*) The power-law dependence only applies in the limit of small energy splitting ΔE, as directly seen from the generalized expression of T_{co} for the crossover from 2CK quantum criticality given by Eq. S7. In practice, we only considered the settings of τ for which $\Delta E < E_{\mathrm{C}}/3 \simeq k_{\mathrm{B}} \times 100\,\mathrm{mK}$ (corresponding to a maximum of 9% relative deviation of T_{co} from the power-law dependence). (*ii*) The Kondo temperature must be sufficiently high with respect to T. Indeed, a universal crossover flow is generally expected only in the limit $T, T_{\mathrm{co}} \ll T_{\mathrm{K}}$. Specifically, a too large difference between $G_{1,(2,)3}(\delta V_{\mathrm{g}} = 0)$ and $G_{2(3)\mathrm{CK}}$ (which occurs if T_{K} is not large enough compared to T) results in a non-negligible gate voltage shift of the crossing point $G_{1,(2,)3}(\delta V_{\mathrm{g}}) = G_{2(3)\mathrm{CK}}/2$. As the gate voltage at the crossing point is used to extract $T_{\mathrm{co}}(\Delta E)$, such a shift would translate into an experimental error. In practice, we therefore only considered the settings of τ for which $|1 - G_{1,(2,)3}(\delta V_{\mathrm{g}} = 0, T)/G_{2(3)\mathrm{CK}}| < 0.25$.

Supplementary text

3   Model, predictions and super-ballistic observation

Multichannel 'charge' Kondo model. The mapping of the circuit Hamiltonian in the weak coupling limit to an anistropic Kondo model is here made explicit, following (*28*). The circuit Hamiltonian for a metallic island coupled through N single-channel point contacts to N different leads is usually written (*28,31*):

$$H = H_I + \sum_{i=1}^{N} \left(H_{Li} + H_{QPCi} \right) + E_{\mathrm{C}} \left(\frac{\hat{Q}}{e} - \frac{Q_0}{e} \right)^2, \tag{S1}$$

with H_I (H_{Li}) the Hamiltonian describing the electron continuum in the island (in the lead i), $\hat{Q}$ the island charge operator, Q_0 a gate voltage dependent charge offset, and H_{QPCi} the Hamitonian describing the electron transfers between island and lead i (across QPC$_i$):

$$H_{QPCi} = t_i \sum_{k,k'} c^+_{Iik'} c_{Lik} + H.c., \tag{S2}$$

where $c_{Iik'(Lik)}$ is the electron annihilation operator in the island (lead) associated with the conduction channel across QPC$_i$ and t_i the coupling coefficient (here assumed independent of Lik and Iik'). Introducing the electrons' 'localization pseudospin-1/2' (s_i) between island (pseudospin state $\downarrow$) and lead i (pseudospin state $\uparrow$), and regarding the island's charge $\hat{Q}$ as an independent macroscopic quantum degree of freedom (which is valid in the continuous

density of states limit, see e.g. (*31*) for a specific discussion), the circuit Hamiltonian reads (see (*19,28,31*) and also (*43*)):

$$H = H_I + \sum_i \left[H_{Li} + N_e t_i (S^+ s_i^- + S^- s_i^+) \right] + E_C \left(\frac{\hat{Q}}{e} - \frac{Q_0}{e} \right)^2 , \qquad (S3)$$

with $S^\pm = \sum_Q |Q \pm 1\rangle \langle Q|$, $s_i^+ = (1/N_e) \sum_{k,k'} c_{Lik}^+ c_{Iik'}$, $N_e \equiv \sqrt{\sum_{k,k'}}$ the effective number of electrons, and $s_i^- = (s_i^+)^\dagger$. For small enough coupling coefficients t_i, the term proportional to E_C in eqs S1 and S3 effectively freezes out all island's charge states in the limit $T \ll E_C/k_B$, except for the two of lowest energy (tuned at degeneracy in the Kondo regime). In this low-temperature limit, the charge states of the island therefore reduce to a pseudospin S of $1/2$, which is flipped by tunneling onto or off the island at each of the QPCs. The terms of the form $S^+ s_i^-$ in Eq. S3 indeed describes a spin exchange between the Kondo impurity charge pseudospin-$1/2$ and the localization pseudospin-$1/2$ of the electrons in continuum i. Note that the Kondo exchange is here proportional to t_i, in contrast with spin Kondo devices based on small quantum dots where spin flips result from virtual, second-order processes. Furthermore, the last term in Eq. S3 reduces to a Zeeman splitting ΔE of the charge pseudospin of $1/2$, with an effective magnetic field that is simply proportional to the gate voltage detuning δV_g from charge degeneracy ($\Delta E = 2E_C|\delta V_g|/\Delta$, for $|\delta V_g| < \Delta/2$ with Δ the gate voltage period of Coulomb oscillations) (*28*). Note that the corresponds to the anisotropic Kondo model, since there is no component $S^z s_i^z$ (in contrast to Eq. 1, where the coupling coefficient J is assumed identical for the x, y and z components). This anisotropy of the coupling is irrelevant in the renormalization group sense as it disappears in the low-temperature limit (*12*). At $T \sim E_C/k_B$, the thermal activation of additional charge states effectively breaks the charge pseudospin-$1/2$ mapping, and thereby provides a high energy cutoff for Kondo physics (for a specific NRG study, see section "charge' Kondo universality' and Fig. S4). Note finally that the experimentally probed electrical conductances across the charge Kondo electronic channels are connected, in usual Kondo language, to two-particle correlation functions (see (*34,35*) and also (*43–45*)). Those correlation functions were calculated exactly at the fixed point by Ludwig and Affleck using conformal field theory (*13*) and, for the 2CK model, as a full function of temperature via NRG in (*19*). In contrast, for previous spin 2CK nanostructures based on small quantum dots (*2,5*) the conductance is proportional to the single-particle $\mathcal{T}$ matrix (*15*).

Multichannel Kondo physics with strongly coupled contacts. Beyond weakly coupled QPCs, quantum fluctuations compete with the freezing of higher energy charge states, which can break the direct mapping of the two lowest energy charge states on a Kondo pseudospin $S = 1/2$ (note that charge quantization breakdown is found and predicted only close to the ballistic limit, see (*30*) for an experimental exploration). Nevertheless, even for nearly ballistic contacts, where many charge states coexist in a quantum superposition, the low-temperature physics at the degeneracy point ($\delta V_g = 0$) as well as the crossover flow from quantum criticality should be universal, indistinguishable from what one expects from the standard $S = 1/2$ multichannel Kondo model. This was shown in (*14*), in particular by map-

ping the circuit Hamiltonian derived for two nearly ballistic channels onto the Hamiltonian obtained by Emery and Kivelson (*7*) for the anisotropic two-channel Kondo model in the Toulouse limit (see below Eq. 53 of (*14*)). It is also attested by the identical expression for the universal conductance flow $\tilde{G}_{2\mathrm{CK}}(T/T_{\mathrm{co}})$ for the crossover from 2CK quantum criticality (given by Eq. S4 with $T/T_{\mathrm{K}} = 0$) derived analytically in both the opposite tunnel and nearly ballistic limits (Eq. 6 in (*19*) and Eq. 38 in (*29*), respectively). Besides these limits, the general case of arbitrary coupling strength was studied numerically (see e.g. (*19,31*) and section "charge' Kondo universality'), further corroborating the robust Kondo character including in the presence of strongly coupled contacts.

Non-Fermi liquid temperature exponents. For $N \geq 2$ Kondo channels and a Kondo impurity of spin $S = 1/2$, observables are naively expected to display the dominant temperature power-law $T^{2/(N+2)}$ in the vicinity of the NCK fixed point (see e.g. (*12*) and references therein). This is however not necessarily the case: different power laws can arise e.g. for observable involving operators in the charge or spin sectors (*12*) or due to a vanishing first order development near the fixed point.

For 2CK ($N = 2$), the Kondo channels conductance in the present 'charge' implementation is predicted to scale linearly ($\Delta G \propto T$), and not as the naively expected $\sqrt{T}$. This prediction was obtained both analytically in the case of a nearly ballistic channel (see Eq. A9 in (*29*), the specific discussion in Methods of (*6*), and Eq. S4 with $T_{\mathrm{co}} = 0$), and from recent NRG calculations starting from the opposite limit of a tunnel contact (*19*). Note the difference with the conductance in previous spin 2CK implementations with small quantum dots, where the naively expected $\sqrt{T}$ was predicted and observed (*2,5*). Indeed, the conductance in these spin Kondo devices is proportional to the single-particle $\mathcal{T}$ matrix (*15*), whereas in the 'charge' implementation it relates to two-particle correlation functions (see (*35*) and also (*43, 45*), or Eq. S10). After submission of this manuscript, three new works calculating the 2CK power law dependence of the conductance in the 'charge' Kondo implementation with different methods appeared (see (*35*) and also (*43, 45*)): a linear behavior is also found in (*35*) and (*43, 45*) (a different T^2 scaling initially obtained in the published article (*45*) was subsequently corrected in an Erratum and also in the second arXiv version).

For 3CK ($N = 3$), the naively expected $T^{2/5}$ is precisely reproduced by the new NRG calculation of the universal 'charge' Kondo conductance curve shown Fig. 4B,C. This is best seen by plotting in a $\log$-$\log$ scale the difference ΔG between this NRG curve and the predicted 3CK fixed point $G_{3\mathrm{CK}} = 2\sin^2(\pi/5)e^2/h$, as shown Fig. S5. Note that the new preprint (*43*) finds a different power law $T^{4/5}$. However, the general prediction $T^{4/(N+2)}$ of (*43*) for arbitrary N also seems in contradiction with previous calculations in the large N limit of the frequency dependence at zero temperature $\omega^{2/(N+2)}$ (see eqs D30 and D11 in appendix D of (*44*)), which instead correspond to the naively expected power law also predicted here by NRG for $N = 3$. In practice, we chose in the manuscript to keep using the NRG prediction $T^{2/5}$, that precisely matches the naive expectation. From an experimental stand point, although the data is closer to $T^{2/5}$, it does not allow to unambiguously rule out $T^{4/5}$ due to the relatively large uncertainty combined with the possibility that observing $T^{4/5}$ requires approaching even closer of the fixed point.

$\mathbb{Z}_N$ **parafermions.** As a guide to the reader, we point out the particularly accessible discussion in the last paragraph of (*43*), which complements the original works (*7,9*). The authors of (*43*) relate the non-Fermi liquid character of the N-channel Kondo fixed point ($N \geq 2$) to the $\mathbb{Z}_N$ parafermionic theory describing the renormalization flow at the generalized Toulouse point. The parafermion charge $e \times (2N - 2)/(N + 2)$ is mentioned and a connection is made with the zero temperature residual entropy at the NCK fixed point ($S = \ln(2\cos[\pi/(N + 2)])$, as indicated in e.g. (*12*) and as also explicitly confirmed in the present context by our NRG calculations).

2CK conductance in near ballistic, low temperature limit ($k_{\mathrm{B}}T \ll E_{\mathrm{C}}$, $1 - \tau_{1,3} \ll 1$)**.** Here, we provide the theoretical expression used to calculate the conductance displayed as a continuous line in Fig. 1C and the universal crossover curve $\tilde{G}_{2\mathrm{CK}}(T/T_{\mathrm{co}})$ shown as a thick dashed line in Fig. 5B. In addition, one can derive from this formula the quantitative theoretical expression of T_{co} for the crossover from 2CK quantum criticality for arbitrary δV_{g} at $1 - \tau \ll 1$ (used in Fig. 5B), and also the 2CK non-Fermi liquid scaling exponent for the conductance $\Delta G \propto T/T_{\mathrm{K}}$ at $\delta V_{\mathrm{g}} = 0$ and $\tau_1 = \tau_3 \equiv \tau$ (Fig. 3), together with the tested functional form $T_{\mathrm{K}} \sim E_{\mathrm{C}}/(1 - \tau)$ (bottom right inset of Fig. 3). The analytical prediction of eqs 38, 26 and A9 in (*29*) give for the overall conductance $g_{1\text{-}3}$ across the two connected $\mathrm{QPC}_{1,3}$ both set to be nearly ballistic, but not necessarily to identical tunings, and for low temperatures $T \ll E_{\mathrm{C}}/k_{\mathrm{B}}$:

$$g_{1\text{-}3} = 1/(1/G_1 + 1/G_3) = \frac{e^2}{2h}\left[1 - \frac{T}{T_{\mathrm{K}}^{\star}} - \int_0^{\infty} \frac{\cosh^{-2}(x)}{1 + (2xT/T_{\mathrm{co}})^2}\mathrm{d}x\right], \qquad \text{(S4)}$$

with

$$T_{\mathrm{K}}^{\star} = \frac{16E_{\mathrm{C}}/\left(k_{\mathrm{B}}\pi^3\exp(\mathbf{C})\right)}{2 - \tau_1 - \tau_3 + 2\sqrt{(1 - \tau_1)(1 - \tau_3)}\cos(2\pi\delta V_g/\Delta)}, \qquad \text{(S5)}$$

$$T_{\mathrm{co}} = \frac{2\exp(\mathbf{C})E_{\mathrm{C}}}{\pi^2 k_{\mathrm{B}}}\left(2 - \tau_1 - \tau_3 - 2\sqrt{(1 - \tau_1)(1 - \tau_3)}\cos(2\pi\delta V_g/\Delta)\right), \qquad \text{(S6)}$$

where $\mathbf{C} \simeq 0.5772$ is the Euler-Mascheroni constant and Δ the gate voltage period of Coulomb oscillations. Note that the numerical prefactor for the scaling Kondo temperature $T_{\mathrm{K}}^{\star}$ in Eq. S5 does not precisely correspond to the convention used in the main article, which is based on the knowledge of the full renormalization flow only accessible through NRG methods (see next section for further discussion). For two symmetric channels $\tau \equiv \tau_1 = \tau_3$ and at charge degeneracy $\delta V_{\mathrm{g}} = 0$, one finds $T_{\mathrm{co}} = 0$ and $T_{\mathrm{K}}^{\star} \propto E_{\mathrm{C}}/(1 - \tau)$. The low temperature criteria $T \ll E_{\mathrm{C}}/k_{\mathrm{B}}$ therefore implies that Eq. S4 is valid only in the asymptotic regime $T \ll T_{\mathrm{K}}^{\star}$, where $\Delta G \propto T$. The universal 2CK crossover curve for the conductance per channel $\tilde{G}_{2\mathrm{CK}}(T/T_{\mathrm{co}})$ (thick dashed line in Fig. 5B) corresponds to $2g_{1\text{-}3}$ as given by Eq. S4 in the limit of negligibly small $T/T_{\mathrm{K}}^{\star}$. Importantly, the universal character of $\tilde{G}_{2\mathrm{CK}}$ is attested by the fact that the exact same expression was obtained in the opposite limit of tunnel contacts $\tau_{1,3} \ll 1$ (Eq. 6 in (*19*)). For two symmetric channels $\tau \equiv \tau_1 = \tau_3$ at arbitrary charge degeneracy δV_{g}, the crossover temperature simplifies into:

$$T_{\mathrm{co}} = 8\exp(\mathbf{C})E_{\mathrm{C}}(1 - \tau)\sin^2(\pi\delta V_g/\Delta)/(k_{\mathrm{B}}\pi^2), \qquad \text{(S7)}$$

which was used to plot the data versus T_{co}/T in the right side of Fig. 5B. Note that the generically expected quadratic dependence of T_{co} with the parameter-space distance to the 2CK quantum critical point is recovered for both small $\delta V_{\mathrm{g}} \ll \Delta$ and small $\Delta\tau \equiv \tau_1 - \tau_3 \ll 1 - \langle\tau_{1,3}\rangle$. The continuous line in Fig. 1C corresponds the conductance $G_{1,3} = 2g_{1\text{-}3}$ calculated with eqs S4, S5, S6 using the separately characterized values $\tau_1 = \tau_3 = 0.9$, $T = 7.9\,\mathrm{mK}$, $E_{\mathrm{C}} = k_{\mathrm{B}} \times 0.3\,\mathrm{K}$ and $\Delta = 0.7\,\mathrm{mV}$, without any fit parameters.

Kondo temperature versus model parameters. Here, we discuss the relationship between scaling/Kondo temperature and microscopic model parameters τ and E_{C}, with a specific focus on the existence of a power-law divergence at a critical setting $\tau = \tau_c$. The first characteristic of the Kondo temperature T_{K} is that it corresponds to the scaling temperature in the universal renormalization flow regime. With such a definition alone, the multiplicative factor of $T_{\mathrm{K}}(\tau, E_{\mathrm{C}})$ is an arbitrary constant value. Following standard practice (*46*), this factor is set such that $G_{1,(2,)3}(T = T_{\mathrm{K}}) = G_{2(3)\mathrm{CK}}/2$. The Kondo temperature therefore also corresponds to the characteristic temperature scale at which Kondo physics develops when starting with a weak Kondo coupling (e.g. $\tau \ll 1$). Beyond initially weak Kondo couplings, $G_{2(3)\mathrm{CK}}/2$ may not be within the explored range of renormalized conductances (e.g. for large τ). However, the scaling Kondo temperature T_{K} can always be adjusted by matching the data in the universality regime ($T \ll E_{\mathrm{C}}/k_{\mathrm{B}}$) with the full universal curve obtained by NRG starting from a weak tunnel coupling. The definition of T_{K} as the scaling Kondo temperature allows for values possibly much larger than $E_{\mathrm{C}}/k_{\mathrm{B}}$. In such cases, T_{K} does not correspond to the temperature scale at which Kondo physics develops since the universal Kondo regime only takes place well below the high-energy cutoff E_{C}. For 2CK, Matveev and Furusaki predict in (*29*) that $T_{\mathrm{K}}(1 - \tau \ll 1, E_{\mathrm{C}}) \propto E_{\mathrm{C}}/(1 - \tau)$, where $\tau_c = 1$ (see previous section). Note that a peaked Kondo temperature at a specific Kondo coupling setting was subsequently predicted for 2CK in (*31,36*). In general (beyond 2CK), the power-law scaling of T_{K} at $|\tau - \tau_c| \ll 1$ can be obtained assuming that the Kondo temperature T_{K} diverges at a critical transmission probability τ_c (in agreement with experimental observation, see insets in figs 3 and 4B). Expanding linearly the channels conductance for $|\tau - \tau_c| \ll 1$, one finds at $T \ll E_{\mathrm{C}}/k_{\mathrm{B}}$:
$$G_i(T) = G_{\mathrm{NCK}} \times \left(1 + A(\tau - \tau_c)(k_{\mathrm{B}}T/E_{\mathrm{C}})^{\alpha}\right), \tag{S8}$$
with A a multiplicative factor of order 1, G_{NCK} the NCK low-temperature conductance fixed point, and α the temperature exponent for the conductance when approaching the Kondo fixed point ($\alpha = 1$ for 2CK , $\alpha = 2/5$ for 3CK). Comparing with the low-temperature Kondo scaling $G_i(T) - G_{\mathrm{NCK}} \propto (T/T_{\mathrm{K}})^{\alpha}$, where all microscopic parameters are encapsulated in T_{K}, directly gives
$$T_{\mathrm{K}}(|\tau - \tau_c| \ll 1) \propto E_{\mathrm{C}}|\tau - \tau_c|^{-1/\alpha}. \tag{S9}$$
This prediction, which is novel for 3CK, is shown as continuous lines in the insets of Fig. 3 using the corresponding theoretical values of α. A close agreement is observed with the data.

Asymptotic crossover limit $\tilde{G}_{\mathrm{NCK}}(T_{\mathrm{co}}/T \ll 1)$. Here we derive the asymptotic functional form at $T_{\mathrm{co}}/T \to 0$ (close to quantum criticality) of the universal conductance curve

$\tilde{G}(T_{\mathrm{co}}/T)$ describing the crossover from NCK Kondo quantum criticality induced by breaking the degeneracy of the charge Kondo pseudospin ($\Delta E \neq 0$, $\Delta \tau = 0$, $T \ll T_{\mathrm{K}}$). These asymptotic functional forms are shown for 2CK and 3CK as grey dash-dotted lines in the right side of Fig. 5B and Fig. 5C, respectively. The limit $T_{\mathrm{co}}/T \to 0$ corresponds to very small gate voltage detuning $\delta V_{\mathrm{g}}/\Delta \ll 1$ (Δ being the gate voltage period). Although the physics is dominated by non-Fermi liquid scalings induced by the NCK quantum critical point, the expansion at $T \neq 0$ of the physical conductance observable with respect to δV_{g} is regular (analytic), as finite temperature regularizes infrared divergences in the corresponding coefficients. From the even symmetry between positive and negative detunings δV_{g}, the first term in this expansion is quadratic in δV_{g}. In the presently considered regime $T \ll T_{\mathrm{K}}$, this reads $\Delta G \equiv G(\delta V_{\mathrm{g}} \to 0) - G_{\mathrm{NCK}} \propto \delta V_{\mathrm{g}}^2$. On the other hand, we generally know that $G(T \ll T_{\mathrm{K}}, \delta V_{\mathrm{g}})$ can be reduced to a universal function $\tilde{G}_{\mathrm{NCK}}$ of the rescaled temperature T/T_{co} (for $T_{\mathrm{co}} \ll T_{\mathrm{K}}$). Moreover, using the analogy between Zeeman splitting of a magnetic impurity and charge pseudospin energy detuning ($\Delta E \propto \delta V_{\mathrm{g}}$), conformal field theory predicts that the crossover temperature scales as $T_{\mathrm{co}} \propto \delta V_{\mathrm{g}}^{(N+2)/N}$ in the limit of small δV_{g} (see e.g. (*12*)). By direct identification, one immediately deduces the power-law asymptotic behavior $\tilde{G}_{\mathrm{NCK}}(T_{\mathrm{co}}/T \ll 1) - G_{\mathrm{NCK}} \propto (T_{\mathrm{co}}/T)^{2N/(N+2)}$. At 2CK, this expression reduces to a linear asymptotic scaling $\tilde{G}_{\mathrm{2CK}}(T_{\mathrm{co}}/T \ll 1) - e^2/h \propto (T_{\mathrm{co}}/T)$, in agreement with the full analytical prediction (Eq. S4, see right side of Fig. 5B). At 3CK, the above asymptotic expression reduces to $\tilde{G}_{\mathrm{3CK}}(T_{\mathrm{co}}/T \ll 1) - G_{\mathrm{3CK}} \propto (T_{\mathrm{co}}/T)^{6/5}$, in agreement with novel NRG calculations (see right side of Fig. 5C).

Super-ballistic conductance. NRG calculations directly show that the emergence of a super-ballistic single-channel conductance follows from the Kondo model. It arises along the non-monotonous renormalization flow towards the 1CK fixed point, when considering the conductance observable in the present 'charge' implementation. Note that a similar observation (although less substantial) was previously made when investigating the 'charge' Kondo renormalization flow with two channels (see Methods in (*6*) for a specific discussion). Experimentally, the opening of a second channel across QPC$_2$ could, in principle, provide a simple explanation for the measurement of a conductance G_2 above e^2/h. However this simple explanation can be directly ruled out, without the need to invoke the NRG confirmation. Firstly, the second and third (inner) quantum Hall edge channels that could possibly be transmitted across QPC$_2$ (the experiment is performed at filling factor $\nu = 3$) are completely reflected, by a large margin, when the first (outer) quantum Hall edge channel is partially transmitted. This is evidenced by the very broad (0.25 V in split gate voltage V_2^{qpc}) and very flat e^2/h plateau, which separates the full opening of the first channel from the point where the second channel starts to open (see inset of Fig. S2E). Secondly, this e^2/h plateau is very robust up to energies much higher than the charging energy $E_{\mathrm{C}} \simeq 26 \, \mu e$V that sets an upper bound for Coulomb and Kondo effects: We checked the plateau robustness up to a dc voltage of $V_{\mathrm{dc}} \simeq 70 \, \mu$V applied directly across QPC$_2$ (we did not try higher values), and found that the plateau remains very precisely at $G_2 = e^2/h$. Moreover, we find that a QPC initially completely closed stays closed even in the presence of the charge Kondo effect (here with two symmetric channels as shown with the $G_2 = 0$ data in Fig. 6, and also with

10

two asymmetric channels in the previous 'charge' Kondo experiment described in (*6*)). In fact, the conductance of a channel that is initially (at high T) less coupled to the island than the other ones is found and predicted to be systematically further suppressed as temperature is reduced (e.g. an hypothetical weakly transmitted second channel across QPC_2, despite the above evidences that there is no such second channel). In contrast, we observe here a large G_2 overshoot, of up to $+0.25e^2/h$ above the free electron quantum limit e^2/h. We now list the specific QPC tunings of $\tau_{1,2,3}$ for which we found a super-ballistic conductance G_2 in Fig. 6 (in the explored temperature range, only including data points for which the statistical uncertainty on G_2 is smaller than $0.1e^2/h$, and with the discrete settings of τ_2 in the indicated ranges as given Fig. S2C): at $\tau_{1,3} \simeq 0.1$ for $\tau_2 \in [0.79, 0.94]$; at $\tau_{1,3} \simeq 0.20$ for $\tau_2 \in [0.64, 0.98]$; at $\tau_{1,3} \simeq 0.34$ for $\tau_2 \in [0.68, 0.98]$; at $\tau_{1,3} \simeq 0.48$ for $\tau_2 \in [0.74, 0.98]$; at $\tau_{1,3} \simeq 0.56$ for $\tau_2 \in [0.79, 0.98]$; at $\tau_{1,3} \simeq 0.64$ for $\tau_2 \in [0.82, 0.98]$; at $\tau_{1,3} \simeq 0.68$ for $\tau_2 \in [0.85, 0.98]$; at $\tau_{1,3} \in \{0.74, 0.79\}$ for $\tau_2 \in [0.90, 0.98]$; at $\tau_{1,3} \in \{0.82, 0.85\}$ for $\tau_2 \in \{0.94, 0.98\}$; at $\tau_{1,3} \in \{0.89, 0.94\}$ for $\tau_2 \simeq 0.98$.

4   Numerics

Numerical renormalization group calculations. Numerical calculations of the universal 2CK and 3CK conductance presented in figs 4,5,6 were performed using a variant of Wilson's numerical renormalization group (NRG) technique (see e.g. (*17*) and (*47*)), adapted to treat the multichannel charge-Kondo Hamiltonian, Eq. S1, in the limit where the island charging energy E_C is the largest energy scale in the problem (including the conduction electron half-bandwidth D; the effect of $E_C < D$ is discussed in the next section). In this case, the two charge states of the island of lowest energy form a pseudospin-$1/2$, while the other charge states can be ignored whatever the QPCs' connection strengths. The resulting anisotropic multichannel Kondo model (Eq. S3 including only the two lower charge states) is solved non-perturbatively with NRG. The conduction electron density for each of the N channels is discretized logarithmically and the system is then mapped onto a 1-dimensional model in which the Kondo pseudospin is connected to one end of the bundle of N semi-infinite 'Wilson chains'. The renormalization group character of the problem is revealed by iterative diagonalization of the chain: the physics at successively lower energy scales is probed at each step as high-lying states are iteratively eliminated. The computational complexity of an NRG calculation scales exponentially with the number of channels, N. Consequently, although standard NRG methods could still be used for 2CK (Fig. 4A,C), the charge-3CK model would have been essentially intractable (large symmetries are broken due to the spin anisotropy inherent to the charge-Kondo setup, and further reduced in the vicinity of the critical point by channel asymmetry and gate detuning of charge degeneracy). This limitation was overcome by using for the 3CK calculations (shown figs 4B,C, 5C and 6) the recently-developed 'interleaved NRG' (iNRG), which makes use of a modified discretization to combine the N Wilson chains into a single generalized chain (*48, 49*). The experimental quantity of interest is the linear response dc differential conductance, whose accurate calculation requires further modification of the standard NRG procedure, as now briefly described. To the Hamiltonian Eq. S1 we add a time-dependent bias term to lead i,

$H_{\text{bias}} = eV_i \hat{N}_{Li} \cos(\omega t)$, where $\hat{N}_{Li} = \sum_k c^+_{Lik} c_{Lik}$ is the total electron number operator for lead i. Measurement of the resulting current into lead j allows determination of elements of the conductance tensor $G_{ij}(T, V_i) = d\langle \hat{I}_j \rangle_T / dV_i$. Within linear response $V_i \to 0$, we employ the Kubo formula (*50*),

$$G_{ij}(T) = \frac{e^2}{h} \lim_{\omega \to 0} \left[\frac{2\pi \hbar^2 \, \text{Im} \, K_{ij}(\omega, T)}{\hbar \omega} \right], \tag{S10}$$

where the limit $\omega \to 0$ yields the desired dc conductance. $K_{ij}(\omega, T)$ is the Fourier transform of the retarded current-current correlator, $K_{ij}(t, T) = i\theta(t)\langle [\dot{N}_{Lj}(t), \dot{N}_{Li}(0)] \rangle$, where $\dot{N}_{L\alpha} = \frac{d}{dt} \hat{N}_{L\alpha}$. In NRG, $K_{ij}(\omega, T)$ is obtained directly on the real axis as an entire function of ω for any T. It is calculated using the full density matrix, established on a complete basis (*51*). However, straight application of this approach is plagued by numerical instabilities: $K_{ij}(\omega, T)$ must be determined very accurately to avoid the spurious divergence of $K(\omega, T)/\omega$ on taking the $\omega \to 0$ limit. Instead, we exploit the identity $\text{Im} \, K_{ij}(\omega, T)/\omega = \omega \text{Im} \, \tilde{K}_{ij}(\omega, T)$, which we derived from equations of motion, where $\tilde{K}_{ij}(t, T) = i\theta(t)\langle [\hat{N}_{Lj}(t), \hat{N}_{Li}(0)] \rangle$. This trick is found to drastically improve the accuracy of the conductance calculation in NRG. It is especially important in the three channel case, whose fixed point conductance takes a nontrivial intermediate value (see (*34*) and also (*43, 44*)). The true 'universal' renormalization flow of the conductance is obtained formally in the scaling limit $k_B T_K / D \to 0$. In practice, we use $\rho t = 0.025$ ($\rho \equiv N_e/2D$, $t \equiv t_{1,(2,)3}$) yielding $T_K \sim 10^{-15} D/k_B$. For 2CK NRG calculations, we used a discretization parameter (*47*) $\Lambda = 3$, retained $N_s = 10000$ states at each step, and averaged the results of $N_z = 4$ calculations. For 3CK iNRG calculations, we used $\Lambda = 3$, $N_s = 38000$, and $N_z = 3$. The three spinful channels, each with U(1) conserved charge, were interleaved, and global U(1) spin symmetry was exploited (note the inherent spin-anisotropy of the charge-Kondo setup).

'Charge' Kondo universality. To what extent does one recover universal Kondo physics at low temperature in the present 'charge' implementation: Does it depend on the channels coupling strength or on the ratio E_C/D? How small does the temperature need to be in practice? We systematically find, based on 2CK NRG calculations, that the universal Kondo scaling curve for the conductance is accurately recovered for $T \lesssim \min(E_C, D)/20k_B$, including when the deduced scaling temperature T_K is large with respect to E_C/k_B or D/k_B. Previous calculations in (*19*) investigated the non-universal behavior resulting from the finite conduction electron bandwidth D, which was assumed to be much smaller than E_C. In that case, whatever the temperature and coupling strengths, only two charge states are accessible and need to be included in the calculation. Here we consider the effect of a finite island charging energy E_C in Eq. S1, which requires going beyond the spin-$\frac{1}{2}$ Kondo paradigm. In practice, 20 charge states are taken into account in the calculations. In Fig. S4, the full universal 2CK conductance scaling curve (black dashed line; two charge states, tunnel contacts) is plotted versus T/T_K and compared to NRG calculations at finite E_C (colored continuous lines; $E_C = 0.1D$ in panel A, $E_C = 0.01D$ in panel B) for different values of the normalized QPCs coupling $\rho t \in \{0.075, 0.10, 0.14, 0.23\}$, with ρ the electronic density of states per unit energy ($\rho \equiv N_e/2D$) and t defined eqs S2,S3. The identical scaling observed for all

values of t at low enough T/T_K, systematically seen also in the opposite regime $D \ll E_C$ (not shown), shows that there exists a temperature $T_{uni}(t, D, E_C)$ below which the measured channels conductance $G_i(T)$ collapses to the same universal Kondo curve when rescaled by T_K – independently of T_K/D, T_K/E_C, E_C/D or ρt. Defining T_{uni} as the temperature below which deviations from universality are smaller than $0.01e^2/h$, we find numerically $k_B T_{uni} \sim E_C/20$ for $E_C < D$, and more generally $k_B T_{uni} \sim \min(E_C, D)/20$. Vertical arrows in Fig. S4 indicate the position of $E_C/20k_B$ in rescaled temperature, with the same color code as the corresponding finite E_C NRG calculation. Note that the pronounced deviations from universality at higher temperature strongly depend on the ratio E_C/D as well as on the number of charge states included in the calculation. While we naively expect a similar universality criterion for 3CK, it should be noted that in this case two different universal curves exist on approaching from below ($\tau < \tau_c$) or above ($\tau > \tau_c$) because the critical 3CK fixed point conductance takes an intermediate value ($0 < G_{3CK} < e^2/h$).

3CK-Fermi liquid crossover. We address the crossover from 3CK quantum criticality induced by an energy splitting $\Delta E \propto \delta V_g$ of the 'charge' Kondo impurity. Is the universal character of the crossover curve $\tilde{G}_{3CK}(T_{co}/T)$ preserved over the full range of gate voltage detuning δV_g, like at 2CK (for 2CK see Eq. S4, derived for near ballistic channels such that $T_K \gg E_C/k_B \gg T_{co}$)? If it is the case, what is the generalized, periodic expression of T_{co} versus arbitrary detuning δV_g (for 2CK, see Eq. S7)? Here, we detail NRG calculations that establish the experimental observation of a robust universality for $\tilde{G}_{3CK}(T_{co}/T)$, for any gate voltage detuning, as well as the generalized expression for the crossover temperature $T_{co} \propto \sin^{5/3}(\pi \delta V_g/\Delta)$ (see Fig. 5C). First, the universal form $\tilde{G}_{3CK}(T/T_{co})$ shown in Fig. 5C was obtained in the standard Kondo limit (retaining just two charge states, and with $T_{co} \ll T_K$). Second, we focus on the more challenging numerical study of the relationship between T_{co} and arbitrary δV_g. This requires to directly calculate the correct form of the full Coulomb peaks (see Fig.1 and Fig. 5B,C), for which one must simulate the effect of finite δV_g over an entire charging period. This involves including many charge states in the calculation (as in the previous section), beyond the standard Kondo model description restricted to the two lower charge states. From analysis of the temperature-dependence of the conductance for a given gate voltage δV_g within these NRG calculations, the crossover scale $T_{co}(\delta V_g)$ could be extracted directly. For 3CK, we find a robust power law $T_{co} \propto \delta V_g^{5/3}$ for small δV_g, as expected from conformal field theory. But for larger δV_g, we find marked deviations, which follow the generalized periodic form $T_{co} \propto \sin^{5/3}(\pi \delta V_g/\Delta)$, to within a numerical accuracy better than 0.5%. This is reminiscent of the periodic variation of the crossover scale in the 2CK model near perfect transmission, as derived analytically by Matveev. We note, however, that no such analytical predictions as yet exist for 3CK, since the critical point is irreducibly interacting. Interestingly, the data (both experimental and numerical) over the entire range of δV_g, when rescaled in terms of this crossover scale T_{co}, fit to the universal form $\tilde{G}_{3CK}(T/T_{co})$ – analogous to the behaviour in the 2CK case. This novel finding extends and strengthens the notion of universality in the 3CK system.
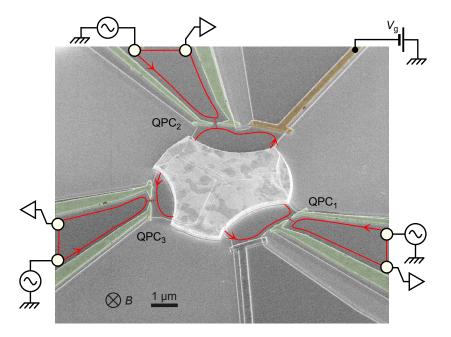
Figure S1: Colored micrograph of the sample, with measurement schematic. The central metallic island (bright) is connected to the circuit through QPCs formed by field effect in a buried two-dimensional electron gas (dark grey) using surface split gates (green). The voltage V_{g}, used to tune the metallic island at charge degeneracy, is applied to a capacitively coupled plunger gate (yellow). Note that the voltages applied to the two lateral gates (yellow and uncolored) are sufficiently negative to deplete the two-dimensional electron gas underneath (except for electronic thermometry and characterization purposes). Due to the strong perpendicular magnetic field $B = 2.7\,\mathrm{T}$, the current propagates along spin-polarized edge channels (red lines) of the integer quantum Hall effect (only the relevant outermost edge channel is shown).
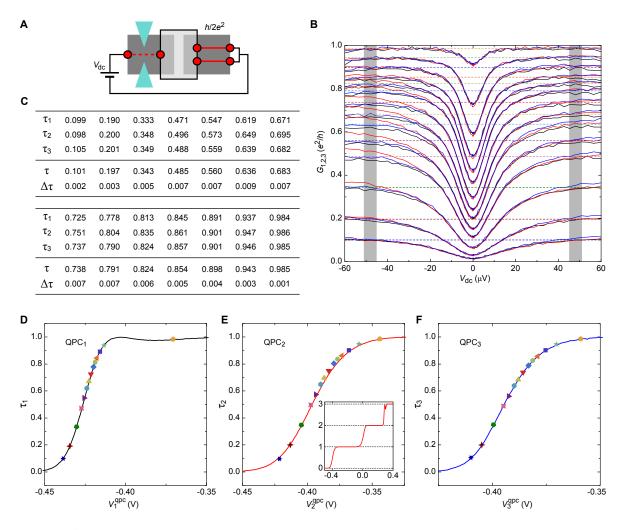
A

B

C

τ_1	0.099	0.190	0.333	0.471	0.547	0.619	0.671
τ_2	0.098	0.200	0.348	0.496	0.573	0.649	0.695
τ_3	0.105	0.201	0.349	0.488	0.559	0.639	0.682
τ	0.101	0.197	0.343	0.485	0.560	0.636	0.683
$\Delta\tau$	0.002	0.003	0.005	0.007	0.007	0.009	0.007
τ_1	0.725	0.778	0.813	0.845	0.891	0.937	0.984
τ_2	0.751	0.804	0.835	0.861	0.901	0.947	0.986
τ_3	0.737	0.790	0.824	0.857	0.901	0.946	0.985
τ	0.738	0.791	0.824	0.854	0.898	0.943	0.985
$\Delta\tau$	0.007	0.007	0.006	0.005	0.004	0.003	0.001

D   **E**   **F**

Figure S2: QPCs characterization. **A**, Schematic circuit used to determine $\tau_{1,2,3}$: a large bias voltage is applied to the characterized QPC in series with a known resistance $h/2e^2$. **B**, Conductance of the QPCs measured at $T = 18\,\mathrm{mK}$ versus dc voltage (continuous lines, black for $\mathrm{QPC_1}$, red for $\mathrm{QPC_2}$ and blue for $\mathrm{QPC_3}$), in the configuration shown in (A) with the series resistance subtracted. The low bias conductance dips result from the dynamical Coulomb blockade, while the high bias plateaus correspond to the 'intrinsic' transmission probabilities $\tau_{1,2,3}$. **C**, The 'intrinsic' transmission probabilities $\tau_{1,2,3}$ at the experimental set points used in the main text are defined as the average of the QPCs conductance on the large bias ranges $\pm[45\,\mu\mathrm{V}, 51\,\mu\mathrm{V}]$ (grey areas in (B)). The individual transmission probabilities $\tau_{1,2,3}$ are averaged to give τ (horizontal colored dashed lines in (B)) and the estimated uncertainty $\Delta\tau$ (the standard error on the mean value τ calculated from six measurements, at negative and positive bias voltage for the three QPCs). **D**, **E**, **F**, The 'intrinsic' transmissions $\tau_{1,2,3}$ of the QPCs are plotted as symbols versus the voltage $V_{1,2,3}^{\mathrm{qpc}}$ applied on one side of the corresponding split gate. The continuous lines are measured using the lateral characterization gates to short-circuit the metallic island for (D),(E), or with $h/2e^2$ in series (see (A)) at an applied bias voltage $V_{\mathrm{dc}} = -50\,\mu\mathrm{V}$ for (F). The inset in (E) shows $\mathrm{QPC_2}$ conductance over a larger gate voltage range including several plateaus, which illustrates the broad separation between channels.
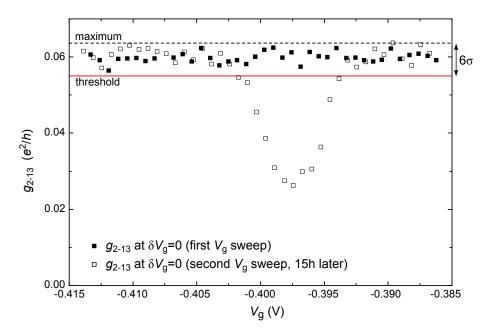
15

Figure S3: Data analysis. The device conductance through QPC_2 ($g_{2-13} \equiv 1/(1/G_2 + 1/(G_1 + G_3))$), measured at charge degeneracy ($\delta V_{\text{g}} = 0$) for $\tau_{1,2,3} \approx 0.1$ and $T \approx 12\,\text{mK}$, is plotted as symbols versus gate voltage V_{g} at the consecutive peak maximums. The same V_{g} sweep (a 1h long measurement) is repeated twice with a 15h time interval. The data points below the statistical threshold shown as a red continuous line are automatically discarded.
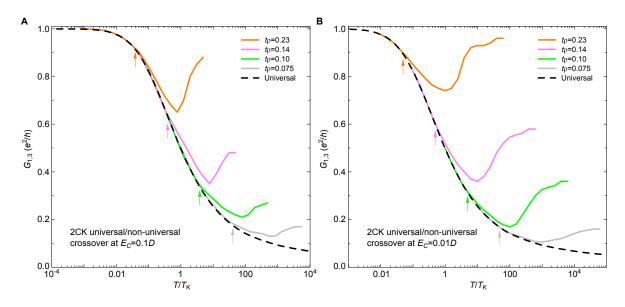
Figure S4: Universality criterion at finite E_{C} and arbitrary QPC couplings. NRG calculations of the 2CK channels conductance $G_{1,3}$ are plotted versus rescaled temperature T/T_{K}. The universal conductance curve shown as a black dashed line (calculated in the regime $k_{\mathrm{B}}T_{\mathrm{K}} \ll D \ll E_{\mathrm{C}}$, i.e. with two charge states and tunnel contacts) is compared to finite E_{C} calculations (colored continuous lines; $E_{\mathrm{C}} = 0.1D$ in panel (A), $E_{\mathrm{C}} = 0.01D$ in panel (B); including twenty charge states of the metallic island in NRG) for different settings of the normalized QPC coupling coefficient $t\rho$ (with t defined Eqs. S2,S3, and ρ the 'effective' electronic density of states). The universality criterion $k_{\mathrm{B}}T_{\mathrm{uni}} \equiv E_{\mathrm{C}}/20$ is pointed out with vertical arrows of the same color as the corresponding NRG calculation at finite E_{C}.
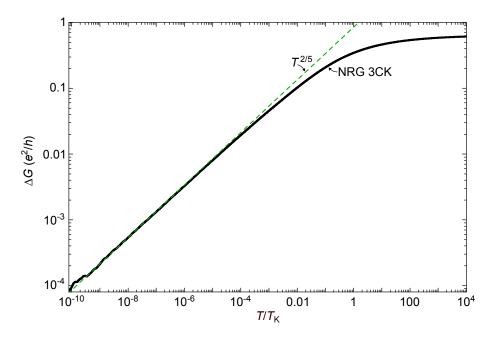
17

Figure S5: 3CK non-Fermi liquid power-law. The $T^{2/5}$ power-law (straight dashed line) naively expected near the 3CK fixed point is compared with the 3CK universal conductance curve calculated by NRG, as a function of the rescaled temperature $T/T_{\rm K}$ in a $\log$-$\log$ scale. The black continuous line displays the difference ΔG between NRG calculation and predicted fixed point $G_{\rm 3CK} = 2\sin^2(\pi/5)e^2/h$.

References and Notes

1. S. Sachdev, *Quantum Phase Transitions* (Cambridge Univ. Press, 2011).

2. R. M. Potok, I. G. Rau, H. Shtrikman, Y. Oreg, D. Goldhaber-Gordon, Observation of the two-channel Kondo effect. *Nature* **446**, 167–171 (2007). doi:10.1038/nature05556 Medline

3. H. T. Mebrahtu, I. V. Borzenets, D. E. Liu, H. Zheng, Y. V. Bomze, A. I. Smirnov, H. U. Baranger, G. Finkelstein, Quantum phase transition in a resonant level coupled to interacting leads. *Nature* **488**, 61–64 (2012). doi:10.1038/nature11265 Medline

4. H. Mebrahtu, I. V. Borzenets, H. Zheng, Y. V. Bomze, A. I. Smirnov, S. Florens, H. U. Baranger, G. Finkelstein, Observation of Majorana quantum critical behaviour in a resonant level coupled to a dissipative environment. *Nat. Phys.* **9**, 732–737 (2013). doi:10.1038/nphys2735

5. A. J. Keller, L. Peeters, C. P. Moca, I. Weymann, D. Mahalu, V. Umansky, G. Zaránd, D. Goldhaber-Gordon, Universal Fermi liquid crossover and quantum criticality in a mesoscopic system. *Nature* **526**, 237–240 (2015). doi:10.1038/nature15261 Medline

6. Z. Iftikhar, S. Jezouin, A. Anthore, U. Gennser, F. D. Parmentier, A. Cavanna, F. Pierre, Two-channel Kondo effect and renormalization flow with macroscopic quantum charge states. *Nature* **526**, 233–236 (2015). doi:10.1038/nature15384 Medline

7. V. J. Emery, S. Kivelson, Mapping of the two-channel Kondo problem to a resonant-level model. *Phys. Rev. B Condens. Matter* **46**, 10812–10817 (1992). doi:10.1103/PhysRevB.46.10812 Medline

8. P. Coleman, L. B. Ioffe, A. M. Tsvelik, Simple formulation of the two-channel Kondo model. *Phys. Rev. B Condens. Matter* **52**, 6611–6627 (1995). doi:10.1103/PhysRevB.52.6611 Medline

9. I. Affleck, M. Oshikawa, H. Saleur, Quantum brownian motion on a triangular lattice and boundary conformal field theory. *Nucl. Phys. B* **594**, 535–606 (2001). doi:10.1016/S0550-3213(00)00499-5

10. P. Nozières, A. Blandin, Kondo effect in real metals. *J. Phys.* **41**, 193–211 (1980). doi:10.1051/jphys:01980004103019300

11. A. C. Hewson, *The Kondo problem to heavy fermions* (Cambridge Univ. Press, 1997).

12. D. L. Cox, A. Zawadowski, Exotic Kondo effects in metals: Magnetic ions in a crystalline electric field and tunnelling centres. *Adv. Phys.* **47**, 599–942 (1998). doi:10.1080/000187398243500

13. I. Affleck, A. W. W. Ludwig, Exact conformal-field-theory results on the multichannel Kondo effect: Single-fermion Green's function, self-energy, and resistivity. *Phys. Rev. B Condens. Matter* **48**, 7297–7321 (1993). doi:10.1103/PhysRevB.48.7297 Medline

14. K. A. Matveev, Coulomb blockade at almost perfect transmission. *Phys. Rev. B Condens. Matter* **51**, 1743–1751 (1995). doi:10.1103/PhysRevB.51.1743 Medline

15. M. Pustilnik, L. Borda, L. I. Glazman, J. von Delft, Quantum phase transition in a two-channel-Kondo quantum dot device. *Phys. Rev. B* **69**, 115316 (2004). doi:10.1103/PhysRevB.69.115316

16. M. Vojta, Impurity quantum phase transitions. *Philos. Mag.* **86**, 1807–1846 (2006). doi:10.1080/14786430500070396

17. R. Bulla, T. A. Costi, T. Pruschke, Numerical renormalization group method for quantum impurity systems. *Rev. Mod. Phys.* **80**, 395–450 (2008). doi:10.1103/RevModPhys.80.395

18. E. Sela, A. K. Mitchell, L. Fritz, Exact crossover Green function in the two-channel and two-impurity Kondo models. *Phys. Rev. Lett.* **106**, 147202 (2011). doi:10.1103/PhysRevLett.106.147202 Medline

19. A. K. Mitchell, L. A. Landau, L. Fritz, E. Sela, Universality and Scaling in a Charge Two-Channel Kondo Device. *Phys. Rev. Lett.* **116**, 157202 (2016). doi:10.1103/PhysRevLett.116.157202 Medline

20. D. Goldhaber-Gordon, H. Shtrikman, D. Mahalu, D. Abusch-Magder, U. Meirav, M. A. Kastner, Kondo effect in a single-electron transistor. *Nature* **391**, 156–159 (1998). doi:10.1038/34373

21. S. M. Cronenwett, T. H. Oosterkamp, L. P. Kouwenhoven, A tunable kondo effect in quantum dots. *Science* **281**, 540–544 (1998). doi:10.1126/science.281.5376.540 Medline

22. J. Nygård, D. H. Cobden, P. E. Lindelof, Kondo physics in carbon nanotubes. *Nature* **408**, 342–346 (2000). doi:10.1038/35042545 Medline

23. M. R. Buitelaar, A. Bachtold, T. Nussbaumer, M. Iqbal, C. Schönenberger, Multiwall carbon nanotubes as quantum dots. *Phys. Rev. Lett.* **88**, 156801 (2002). doi:10.1103/PhysRevLett.88.156801 Medline

24. L. I. Glazman, M. E. Raikh, *JETP Lett.* **47**, 452 (1988).

25. T. K. Ng, P. A. Lee, On-site Coulomb repulsion and resonant tunneling. *Phys. Rev. Lett.* **61**, 1768–1771 (1988). doi:10.1103/PhysRevLett.61.1768 Medline

26. Y. Oreg, D. Goldhaber-Gordon, Two-channel Kondo effect in a modified single electron transistor. *Phys. Rev. Lett.* **90**, 136602 (2003). doi:10.1103/PhysRevLett.90.136602 Medline

27. S. Florens, P. Simon, S. Andergassen, D. Feinberg, Interplay of electromagnetic noise and Kondo effect in quantum dots. *Phys. Rev. B* **75**, 155321 (2007). doi:10.1103/PhysRevB.75.155321

28. K. A. Matveev, *Sov. Phys. JETP* **72**, 892 (1991).

29. A. Furusaki, K. A. Matveev, Theory of strong inelastic cotunneling. *Phys. Rev. B Condens. Matter* **52**, 16676–16695 (1995). doi:10.1103/PhysRevB.52.16676 Medline

30. S. Jezouin, Z. Iftikhar, A. Anthore, F. D. Parmentier, U. Gennser, A. Cavanna, A. Ouerghi, I. P. Levkivskyi, E. Idrisov, E. V. Sukhorukov, L. I. Glazman, F. Pierre, Controlling charge quantization with quantum fluctuations. *Nature* **536**, 58–62 (2016). doi:10.1038/nature19072 Medline

31. E. Lebanon, A. Schiller, F. B. Anders, Coulomb blockade in quantum boxes. *Phys. Rev. B* **68**, 041311 (2003). doi:10.1103/PhysRevB.68.041311

32. Materials and methods are available as supplementary materials.

33. Z. Iftikhar, A. Anthore, S. Jezouin, F. D. Parmentier, Y. Jin, A. Cavanna, A. Ouerghi, U. Gennser, F. Pierre, Primary thermometry triad at 6 mK in mesoscopic circuits. *Nat. Commun.* **7**, 12908 (2016). doi:10.1038/ncomms12908 Medline

34. H. Yi, C. L. Kane, Quantum Brownian motion in a periodic potential and the multichannel Kondo problem. *Phys. Rev. B* **57**, R5579–R5582 (1998). doi:10.1103/PhysRevB.57.R5579

35. L. Landau, E. Cornfeld, E. Sela, Charge fractionalization in a Kondo device. arXiv:1710.03030 [cond-mat.mes-hall] (2017).

36. C. Kolf, J. Kroha, Strong versus weak coupling duality and coupling dependence of the Kondo temperature in the two-channel Kondo model. *Phys. Rev. B* **75**, 045129 (2007). doi:10.1103/PhysRevB.75.045129

37. R. Krishna Kumar, D. A. Bandurin, F. M. D. Pellegrino, Y. Cao, A. Principi, H. Guo, G. H. Auton, M. Ben Shalom, L. A. Ponomarenko, G. Falkovich, K. Watanabe, T. Taniguchi, I. V. Grigorieva, L. S. Levitov, M. Polini, A. K. Geim, Superballistic flow of viscous electron fluid through graphene constrictions. *Nat. Phys.* **13**, 1182–1185 (2017). doi:10.1038/nphys4240

38. H. Guo, E. Ilseven, G. Falkovich, L. S. Levitov, Higher-than-ballistic conduction of viscous electron flows. *Proc. Natl. Acad. Sci. U.S.A.* **114**, 3068–3073 (2017). doi:10.1073/pnas.1612181114 Medline

39. G. Kotliar, D. Vollhardt, Strongly Correlated Materials: Insights From Dynamical Mean-Field Theory. *Phys. Today* **57**, 53–59 (2004). [doi:10.1063/1.1712502](doi:10.1063/1.1712502)

40. K. Le Hur, Coulomb blockade of a noisy metallic box: A realization of Bose-Fermi Kondo models. *Phys. Rev. Lett.* **92**, 196804 (2004). doi:10.1103/PhysRevLett.92.196804 Medline

41. S. Jezouin, F. D. Parmentier, A. Anthore, U. Gennser, A. Cavanna, Y. Jin, F. Pierre, Quantum limit of heat flow across a single electronic channel. *Science* **342**, 601–604 (2013). doi:10.1126/science.1241912 Medline

42. H. Grabert, M. H. Devoret, Eds., Single charge tunneling (1992), plenum, new york edn.

43. Z. Bao, F. Zhang, Quantum Hall charge Kondo criticality. arXiv:1708.09139 [cond-mat.str-el] (2017).

44. H. Yi, Resonant tunneling and the multichannel Kondo problem: Quantum Brownian motion description. *Phys. Rev. B* **65**, 195101 (2002). doi:10.1103/PhysRevB.65.195101

45. M. Pustilnik, B. van Heck, R. M. Lutchyn, L. I. Glazman, Quantum Criticality in Resonant Andreev Conduction. *Phys. Rev. Lett.* **119**, 116802 (2017). doi:10.1103/PhysRevLett.119.116802 Medline

46. H. Zheng, S. Florens, U. Baranger, Transport signatures of Majorana quantum criticality realized by dissipative resonant tunneling. *Phys. Rev. B* **89**, 235135 (2014). doi:10.1103/PhysRevB.89.235135

47. D. Goldhaber-Gordon, J. Göres, M. A. Kastner, H. Shtrikman, D. Mahalu, U. Meirav, From the Kondo Regime to the Mixed-Valence Regime in a Single-Electron Transistor. *Phys. Rev. Lett.* **81**, 5225–5228 (1998). doi:10.1103/PhysRevLett.81.5225

48. K. G. Wilson, The renormalization group: Critical phenomena and the Kondo problem. *Rev. Mod. Phys.* **47**, 773–840 (1975). doi:10.1103/RevModPhys.47.773

49. A. K. Mitchell, M. R. Galpin, S. Wilson-Fletcher, D. E. Logan, R. Bulla, Generalized Wilson chain for solving multichannel quantum impurity problems. *Phys. Rev. B* **89**, 121105 (2014). doi:10.1103/PhysRevB.89.121105

50. K. Stadler, A. Mitchell, J. von Delft, A. Weichselbaum, Interleaved numerical renormalization group as an efficient multiband impurity solver. *Phys. Rev. B* **93**, 235101 (2016). doi:10.1103/PhysRevB.93.235101

51. W. Izumida, O. Sakai, Y. Shimizu, Many Body Effects on Electron Tunneling through Quantum Dots in an Aharonov-Bohm Circuit. *J. Phys. Soc. Jpn.* **66**, 717–726 (1997). doi:10.1143/JPSJ.66.717

52. A. Weichselbaum, J. von Delft, Sum-rule conserving spectral functions from the numerical renormalization group. *Phys. Rev. Lett.* **99**, 076402 (2007). doi:10.1103/PhysRevLett.99.076402 Medline